THESIS FOR THE DEGREE OF LICENTIATE OF ENGINEERING

High Performance Aluminium Alloys for Laser Powder Bed Fusion: Alloy Design and Development

BHARAT MEHTA

Department of Industrial and Materials Science

CHALMERS UNIVERSITY OF TECHNOLOGY

Gothenburg, Sweden 2021

High Performance Aluminium Alloys for Laser Powder Bed Fusion: Alloy Design and Development
BHARAT MEHTA

Technical report on IMS-2021-21

Department of Industrial and Materials Science
Chalmers University of Technology
SE-41296 Gothenburg
Sweden
Telephone +46 (0)31-772 1000

Chalmers digitaltryck
Gothenburg, Sweden 2021

High Performance Aluminium Alloys for Laser Based Powder Bed Fusion: Alloy Design and Development

BHARAT MEHTA
Department of Industrial and Materials Science
Chalmers University of Technology

Abstract:

Additive Manufacturing (AM), particularly Laser Based Powder Bed Fusion (LB-PBF) has proven to be a notable technology to produce novel microstructures and expand the ceiling of product design. However, the development of novel alloys in metal LB-PBF has not followed the same pace as development of product design. The commonly available Fe-, Al- or Ni- alloys are developed from their conventional cast / wrought counterparts with limited knowledge of their processability and adaptability to the LB-PBF process. There is limited research into developing new alloys by the means of pushing the boundaries of conventional metallurgy with help from computational tools available.

This research work focuses on addressing these limitations by working within aluminium alloy systems. It was seen that the prominence of printability issues such as solidification cracking becomes a major hinderance to developing fully dense materials. Alloys processed using LB-PBF were more susceptible to these issues due to the processing conditions, even though the same conditions could make them more desirable in some cases. Thus, simple ways to screen the alloy systems before printing could be used as a quick method to save time. Additionally, the major benefit of LB-PBF comes from rapid solidification wherein solidification rates of few orders of magnitude higher than cast/ wrought alloys are achieved. This can be leveraged to develop new families of Al-alloys, by utilising higher supersaturation of the transition series elements. A few examples are Manganese (Mn), Chromium (Cr) and Zirconium (Zr), which are shown to successfully create printable alloys with solubilities beyond equilibrium.

Printability and high solubility in solid solution of the alloys present a partial solution to the problem. The objective of this study was to showcase high performance Al-alloys, in this case high temperature performance. Mn, Cr and Zr were thus chosen due to their slow bulk diffusivities in aluminium. This means that the nucleation and growth kinetics of the precipitates generated by these elements could be slower than precipitates rich in elements such as Mg and Si. Such an occurrence is lucrative while developing precipitation hardened alloys as the optimum conditions for peak hardness can be controlled relatively easily and improved mechanical properties at high temperature could be expected. Interestingly, it was observed that Al-Mn family of precipitates preferentially grow at grain boundaries in the beginning of heat treatments and later shift to bulk growth. The growth of Al_3Zr precipitates, which occurs in the bulk, could be controlled by optimising the kinetics of growth of these Al-Mn family of precipitates. This phenomenon has experimentally shown to provide a secondary hardening in the alloys and reach hardness values corresponding to that of high strength Al-alloys. This phenomenon is novel for Al-alloys as it would be difficult to recreate the same conditions via other processing routes due to significantly lower solubility of transition elements.

Keywords: Additive Manufacturing, Laser Based Powder Bed Fusion, Aluminium Alloys, Heat Treatment, Precipitation Kinetics, Integrated Computational Materials Engineering

Preface

The work presented in this licentiate thesis was conducted at the Department of Industrial and Materials Science at Chalmers University of Technology between June 2019 and October 2021. The work was conducted within the framework of the Center for Additive Manufacturing – Metal (CAM^2), supported by VINNOVA and ALL-Light project, a part of SIP LIGHTer also supported by VINNOVA. The support from Chalmers Production Area of Advance is acknowledged as well. This research has been carried out under the supervision of Professor Lars Nyborg, Adjunct Professor Karin Frisk and Professor Eduard Hryha.

List of Appended Publications:

Paper I: **Novel Al-Mn based alloys for laser powder bed fusion: alloy design, printability, and microstructure**
B. Mehta, L. Nyborg, K. Frisk, E. Hryha
Manuscript, submitted for publication

Paper II: **Precipitation kinetics and microstructural properties of novel Al-Mn-Cr-Zr based alloys developed for laser powder bed fusion**
B. Mehta, L. Nyborg, K. Frisk
Manuscript, to be submitted

Paper III: **Laser-powder bed fusion of an Al-Mg-Sc-Zr alloy: Manufacturing, Mechanical and High Temperature Properties**
B. Mehta, A. Svanberg, L. Nyborg
Manuscript, submitted for publication

Contribution to Appended Publications:

Paper I: The author planned and performed most of the experimental work and analysis of the results. The author wrote the paper in collaboration with the co-authors.

Paper II: The author planned and performed most of the experimental work and analysis of the results. The author wrote the paper in collaboration with the co-authors.

Paper III: The author planned and performed some of the experimental work and most of the analysis of the results in collaboration with co-authors. The author wrote the paper in collaboration with the co-authors.

Other publications and patent applications not appended in this thesis:

Paper: Effect of Surface Sandblasting and Turning on Compressive Strength of Thin 316L Stainless Steel Shells Produced by Laser Powder Bed Fusion
B. Mehta, E. Hryha, L. Nyborg, F. Tholence, E. Johansson
Metals 11 (7), 2021 https://doi.org/10.3390/met11071070

Patent: New powder, method for additive manufacturing of components made from the new powder and article made therefrom, **EP20212934**
K. Frisk, S. Bengtsson, L. Nyborg, B. Mehta
Priority date: 10 December'2020, Under process

Table of Contents

Chapter 1 – Introduction

According to ISO-ASTM 52900 [1], additive manufacturing (AM) is defined as the process of joining materials to make parts from 3D model data, usually layer upon layer, as opposed to subtractive manufacturing and formative manufacturing methodologies. Such layer upon layer approach makes it possible to develop complex components such as lattice structures or components with bionic design, which helps pushing the boundaries of component design, thus creating better products [2, 3]. Laser based powder bed fusion (LB-PBF) for metals is an AM method where a focused laser beam is used for selective layer wise melting a layer of metal powder to build components layer upon layer [4]. It is therefore possible to achieve rapid cooling rates (up to 10^5 K/s) by leveraging this processing method, thus making it distinct from conventional cast or wrought products. The mechanical properties of AM produced alloys in some cases are seen to be better than their conventionally manufactured counterparts [5, 6, 7]. This is attributed to a different in processing route creating different materials in principle. This means that there is a strong need to develop materials suitable for AM processing to arrive at consistent material properties. This can be done in two ways: tuning currently available alloy compositions or developing entirely new compositions. First, the known alloy compositions for grades useful for certain products could be tuned to become processable via LB-PBF. This could be done by removing alloying elements which could cause formation of unwanted defects such as solidification cracking or adding new elements which can help in improving printability and mechanical properties of the material. Second, entirely new compositions could be developed, which leverage the process to achieve high performance by means of alloy design that is tuned to specific condition in LB-PBF. A fundamental principle for the latter approach would be to understand the limits of processability connected to increased supersaturation for substitutional elements owing to the inherently high cooling rates prevailing in LB-PBF.

Aluminium (Al) alloys are famous for their versatility derived from hundreds of alloying grades [8]. Most alloys are classified into non-heat treatable and heat-treatable alloys, whereby their wrought and cast variants are designated according to the main alloying element. The common alloying elements used are Silicon (Si), Magnesium (Mg), Zinc (Zn), Manganese (Mn), and Copper (Cu). Furthermore, aluminium is known for its age hardenability. This means that after producing an aluminium component, it's mechanical properties can be tweaked via heat treatments to reach significantly higher strengths (500-600 MPa) as compared to pure Al (15-20 MPa). Among the wrought variants, this applies to 2xxx, 6xxx and 7xxx series alloys. This helps aluminium alloys reach specific strength comparable to that of high-strength steel as density for aluminium is nearly one-third that of steels; effectively making the age-hardenable aluminium alloys a great fit for light-weight applications in aircrafts, robots etc. [9, 10]. Despite the availability of several alloys to choose from, aluminium as an alloy is quite hard to produce using LB-PBF. One of the reasons is solidification cracking (or hot cracking), which arises close to the complete solidification of liquid aluminium when there is difference in shrinkage of surrounding solid due to solutes segregating in the liquid [11, 12, 13]. This creates a situation where there is insufficient time to fill the gap between two solidifying Al-grains with the melt, thus creating grain boundary cracking/ decohesion. Such a phenomenon gets worse in LB-PBF as the time taken to achieve complete solidification reduces significantly. Additionally, traditional alloying elements such as Mg and Zn are used in aluminium as they form low temperature intermetallic phases (Mg_2Si or $MgZn_2$) which can then be re-dissolved during heat treatments (called solutioning) and quenched in water to later precipitate as hardening phases with low temperature ageing. However, due to their low evaporation temperature (1363 K for Mg and 1180 K for Zn), these elements are susceptible to evaporation during the LB-PBF process, thus making their use hard [12]. A solution to this problem is to use alloys which are weldable and contains less amount of low evaporating elements, as welding alloys are usually resistant to solidification cracking.

This was one of the reasons behind developing AlSi10Mg or AlSi7Mg, which are the best known commercially available aluminium alloys for LB-PBF [14, 15]. The issue with these alloys is that they do not retain high strength after heat treatments (~250 MPa yield strength [16]). This makes these alloys inadequate for applications demanding higher yield strengths close to ~400 MPa. There have been some alloys for example Scalmalloy® [17], AddAlloy™ [18] and Al-Mn-Sc alloy [19, 20], which utilise the LB-PBF processing to attain high strengths using heat treatments with use of Sc, Zr as alloying elements. However, there seems to be fewer uses of available thermodynamic approaches to help develop a framework for completely new alloy chemistries, as it has been shown possible [21, 22]. Still, the application of thermodynamics modelling combined with the assessment of extended solid solubility to set appropriate alloy systems constitute a way forward to explore the limits for processability in LB-PBF. Having such a framework, powdered material can be designed and its processing into high quality build can be realised. Hence, this thesis study has been framed to develop a framework for utilising Mn, Cr, and Zr as potential alloying elements. A new family of such alloys has thereby been developed and powder has been fabricated. The printability with intended supersaturation in solid solution with resistance to solidification cracking has been demonstrated. With the retained supersaturation, direct hardening response towards attractive mechanical properties is demonstrated. Combined with high throughput microstructural and modelling of precipitation nucleation and growth, the precipitation reaction responsible for the observed age-hardening response are studies. In essence, the alloys studied are shown to have a good direct ageing hardening and also show tentative suitability for high temperature properties as they tend to retain their hardness up to 523-573 K based on current experiments.

1.1 Research Objectives

This thesis study aims at demonstrating how Al-alloys can be tailored for LB-PBF. The approach is developed by combining the available thermodynamic information for a certain alloy system with knowledge of LB-PBF process. This has been then utilized to push supersaturation capabilities and the role of different strengthening mechanisms. Specific research questions in focus of the thesis study are as follows.

a. How to design Al-alloys for LB-PBF coupled for specific application performance?
b. How can alloy compositions be chosen to meet the set design criteria?
c. How can a screening method be developed to avoid issues such as solidification cracking in Al-alloys for LB-PBF?

Chapter 2 – Background

The background chapter introduces the reader to the general understanding of different technologies, processes, and material aspects. The purpose of this chapter is to assist with the comprehension of terms used in the course of this thesis work.

2.1 Additive Manufacturing

The Additive Manufacturing (AM) technology is versatile in terms of how materials are processed with the common theme being a layer-by-layer deposition of material to build three dimensional components. Near net shape components are achieved in this way using AM, thus reducing wastage of materials significantly [4, 23]. As per ISO/ASTM 52900 [1], AM processes can be divided into seven different categories:

1. VAT photopolymerization
2. Powder bed fusion
3. Material extrusion
4. Material jetting
5. Binder jetting
6. Directed energy deposition
7. Sheet lamination

This thesis covers metallic alloys developed for powder bed fusion, in particular laser-based powder bed fusion. The focus of material development is novel high performance aluminium alloys specifically tailored to this AM process.

2.2 Laser Based Powder Bed Fusion of Metals

2.2.1 Introduction

Laser-based powder bed fusion (LB-PBF) involves a focused laser beam with small spot size (typically 40-100 µm), which is controlled using scanning mirrors to steer and reflect the laser beam to selectively melt a region in the build chamber. Layer by layer processing enables the possibility to create complicated shapes and thus push the boundaries of product design; furthermore, it enables the possibilities to produce lattice structures or bionic components [2, 3]. The LB-PBF products can sometimes be designed in a way that they are nearly impossible to be manufactured using conventional manufacturing techniques, which is popularly referred to as "complexity for free" via AM. As illustrated in Figure 1, LB-PBF can provide highly complex components at relatively constant cost. In addition, when the lot size is smaller, such technology is lucrative as the individual component cost stays constant over lot size.

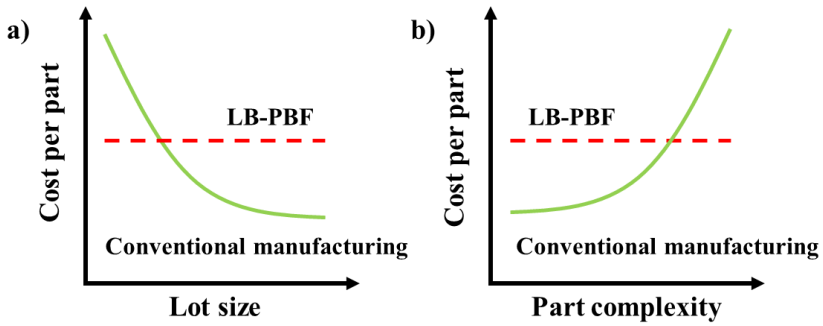

Figure 1 Comparison of LB-PBF process to conventional manufacturing in terms of a) Lot size v/s cost b) Part complexity v/s cost. Redrawn from [24]

2.2.2 Working Principle

Parameters such as laser speed, laser power and layer thickness etc. are varied to control the densification of components during printing. The build chambers vary in shapes and sizes, depending on application although all of them contain a flow of inert atmosphere; typically N_2 or Ar. They could be small as in EOS® M100 machine with a smaller chamber (100 mm diameter x 100 mm height) to large chambers in machines such as SLM® 800 machine (500 mm x 280 mm x 850 mm).

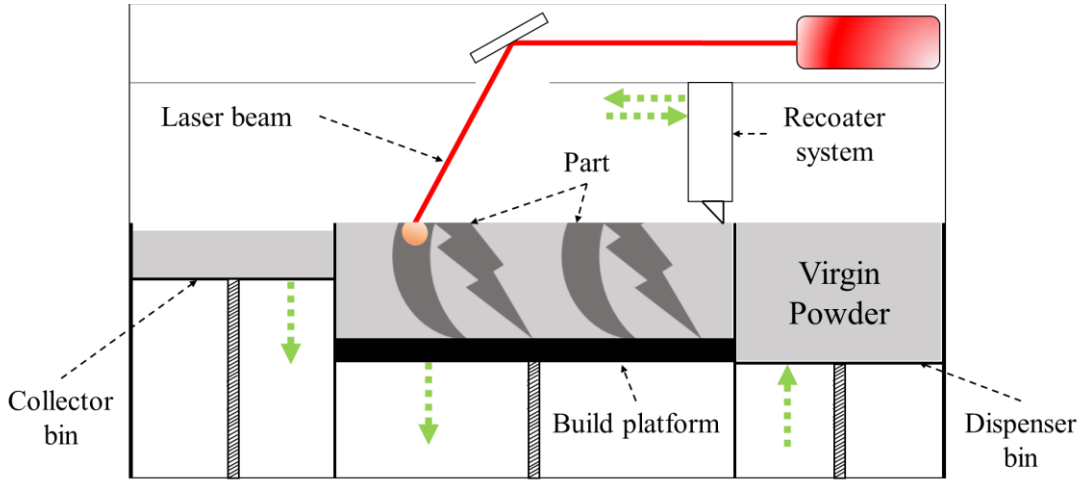

Figure 2 Simple schematic of a typical LB-PBF system. The powder is depicted in light grey colour. The green arrows demarcate the movement of designated components during a typical printing cycle.

A schematic for a typical LB-PBF system is depicted in Figure 2. It shows that the virgin powder is kept in dispenser bin. The recoating system spreads a layer of metal powder (typically 20-100 µm) over the build plate; the recoating system consists of a blade made with high-speed steel, carbon brush etc. to spread a consistent layer of powder. The excess powder goes to the collector bin. After the laser beam selectively melts the component layer by layer on the build platform, the build platform moves down for the recoater system to come back to original position and start by adding another layer of powder till this cycle repeats for several times to complete the fabrication of the component. Consequently, the layer thickness in LB-PBF refers to the movement of the build platform in each stage of the layered processing and not to the actual powder layer thickness being created.

2.2.3 Powder for LB-PBF

Metal powder for LB-PBF systems is typically produced by a method known as gas atomisation. In this process, molten metal is introduced in an inert atmosphere of typically N_2 or Ar, with the impingement of jet of the same gas, which breaks up the melt in sequence into liquid metal droplets, which then solidify into solid particles under the forced cooling conditions in the atomising chamber. Subsequently, the powder is classified to a certain size range depending on the application [25]. A simple schematic for the gas atomisation process is shown in Figure 3.

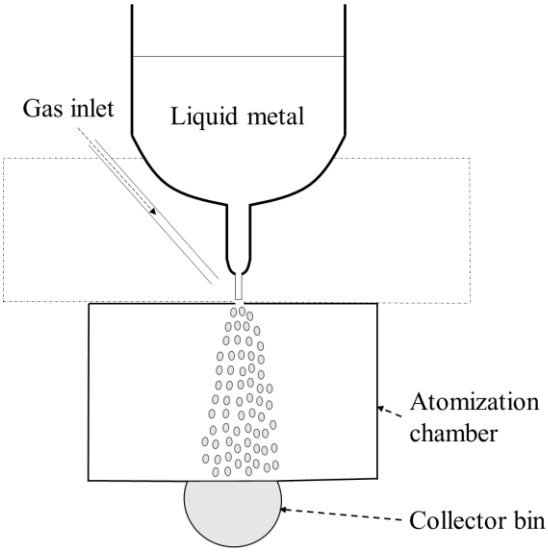

Figure 3 Schematic of gas atomisation. Redrawn from [24]

Normally for LB-PBF processing, powders sizes of between 20-53 µm is achieved with spherical or near spherical morphology. The powder is tuned to required size distribution, packing density and low costs [24]. The typical appearance of gas atomised Al-alloy powder of selected grade (Al-Mn-Cr-Zr) is shown in Figure 4 with its particle size distribution.

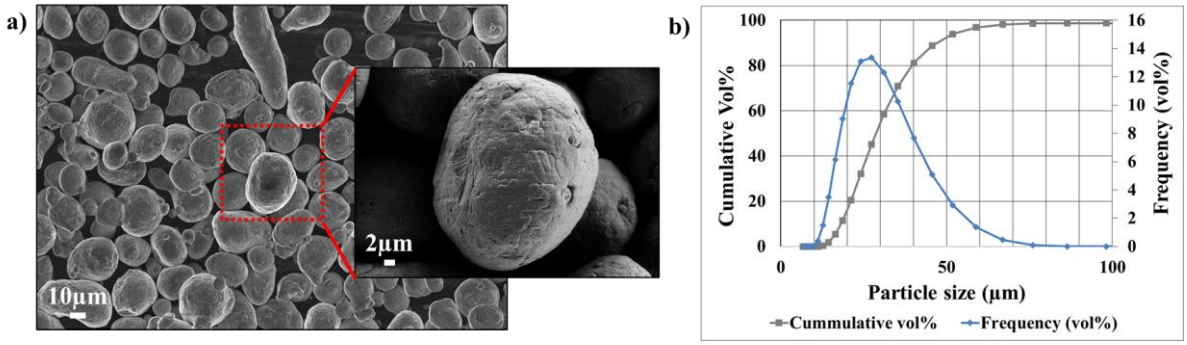

Figure 4 a) Electron microscopy image for Al-Mn-Cr-Zr alloy showing spherical powder with dendritic solidification structure b) Particle size distribution for the same powder in virgin condition.

The particle morphology, size distribution and flowability are important characteristics for ensuring good quality parts. For example, powder of too small size or having non-spherical morphology may show worse powder layer density, thus producing poorer parts with lower part density [26, 27]. Secondly, powder reuse becomes equally important as reuse of powder, especially aluminium could be prone to moisture pickup or spatter generated during printing could make its way into re-sieved powder thus effecting the microstructure of the printed components [28, 29, 30]. This topic is subject of current research and is still to be understood.

2.2.4 Microstructure Developed by LB-PBF

The microstructure developed in LB-PBF are in several ways analogous to that seen in welding; in both cases there is a moving heat source, fusion zone and heat affected zone [31, 32], with the possible distinction that LB-PBF can be fine scale multilayer welding process with all its implications. A simple schematic for the LB-PBF process shown in Figure 5 reflects how the laser source acts as a heat source, with the remelted region as fusion zone and heat affected zone where precipitation may occur due to limited solubility of certain solutes in Al-solid solution. The LB-PBF process means that the material being fabricated is made up of melt pools of 100-200 µm in depth whereas the layer thickness is in typical cases 20-100 µm. This means that several layers are remelted with every layer being printed.

This thermal history as in any multi-pass technology always creates a fresh heat affected zone right below and around the last created melt pool across the part being built.

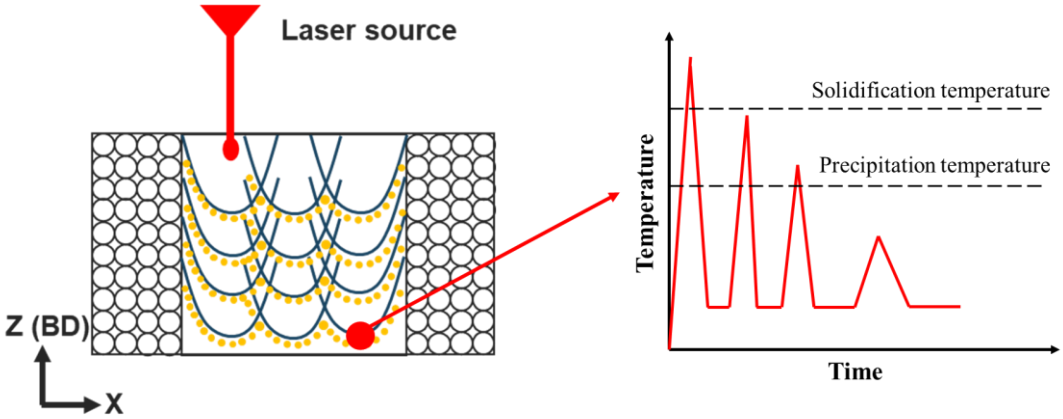

Figure 5 Schematic of LB-PBF process showing remelting effect, forming melt pool boundary precipitates. The graph shows the thermal history at a selected region at melt pool boundary. Inspired from [4]

Furthermore, the solidification structures in LB-PBF (planar, cellular, or dendritic) are supposedly more analogous to welding than casting. As shown in Figure 6 a), the solidification structure can be depicted by temperature gradient at solid-liquid interface (G_L, K/mm units) and solidification rate of the solidification interface (R, mm/s units). The product of G_L and R represents the cooling rate (K/s) which is of the order of 10^3-10^5 K/s, this is higher by a few orders of magnitude than compared to conventional manufacturing such as casting [4]. Composition has a strong role in solidification structure as well, as shown in Figure 6 b), being connected to so-called constitutional supercooling effect. A pure metal (if such would practically exist) would solidify in planar mode, whereas the presence of other alloying elements or impurities (which is true for most metallic alloys) will lead to segregation thus meaning cellular/ dendritic solidification structures. The solute segregation, as defined by ratio of concentration of solute in solid to liquid is represented by partitioning coefficient (k). This coefficient tells whether a solute is to be enriched in liquid (k<1) or solid (k>1) during the cooling [32]. Some elements (such as Mn [33] with k~1) are less prone to such segregation and hence thought to be preferable when it comes to avoiding creation of solute-driven retention of liquid towards the end of solidification process. Higher product of G_L and R would mean that the solidification structure would be finer irrespective of its actual solidification morphology, be it cellular or dendritic. For dendritic solidification, this is illustrated in Figure 7 a). The inset in the figure for this near eutectic Al-Si alloy shows the dendritic structure with clear indication of secondary dendrite arms for the top left part. This secondary dendrite arm spacing is a direct marker for the cooling rate as it relates to the time spent between the liquidus and solidus upon cooling. Also, the primary dendrite arm spacing can depict the cooling rate in a similar way. For cast alloys, typical arm spacing are 10-100 µm [34]; for LB-PBF alloys that the arm spacing can be down to 0.1-10 µm which is in the range that can be observed for gas-atomised powder [35]. This conveys the correlation to finer solidification structure formed owing to high cooling rates. For secondary dendrite arm spacing (SDAS), the corelation is shown in Equation 1 [36].

$$\boldsymbol{\lambda = \lambda_o . R^{-n}} \quad (1)$$

The parameters in the equations above are as follows.

$\boldsymbol{\lambda}$	=	secondary dendrite arm spacing (SDAS)
$\boldsymbol{\lambda_o}$, $\boldsymbol{n}$	=	material dependent constants
$\boldsymbol{R}$	=	cooling rate

For cellular solidification as well as for primary dendrites same principal equation applies although the constants change. Furthermore, when temperature gradients are higher or solidification rates are small enough, a cellular solidification front may prevail. Figure 7 b) illustrates a cellular solidification pattern

observed in Al-Mn-Cr-Zr alloys printed using LB-PBF process, where the precipitates align themselves inside the prior melt pools in arrays along the solidification front direction, which follows the heat source, in this case being the laser. Precipitates further grow at melt pool boundaries, but this phenomenon is connected to the heat affected zone effect as discussed previously.

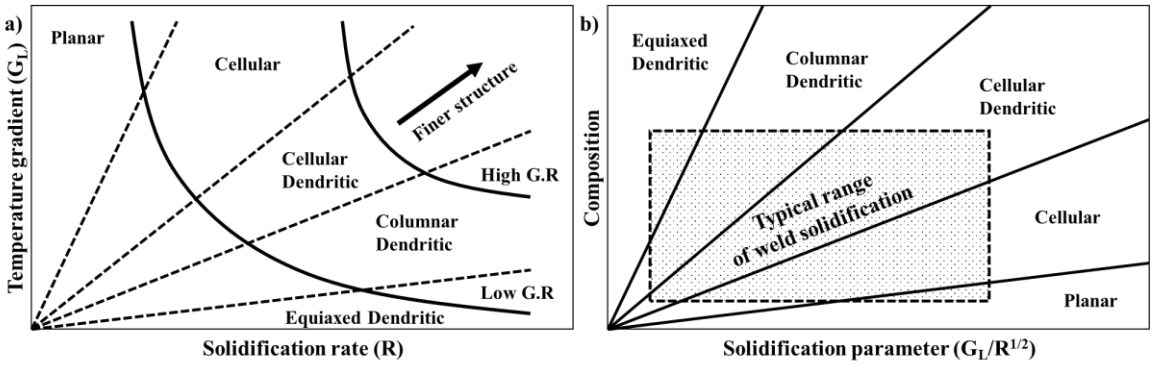

Figure 6 a) Schematic for temperature gradient (G_L) vs solidification rate (R) showing various solidification structures possible b) Schematic for composition vs solidification parameter ($G_L/R^{1/2}$) showing various solidification structures and where typical welding range lie. Drawn from [32]

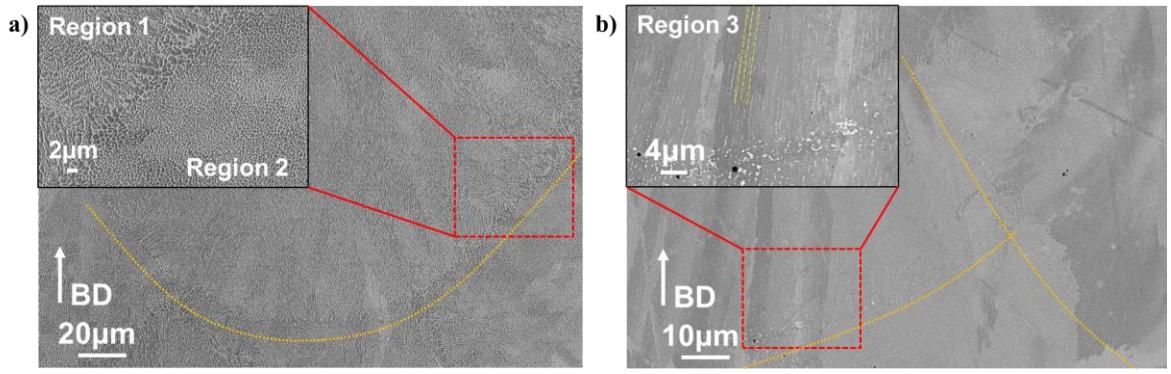

Figure 7 Electron microscopy images of two Al-alloys printed using LB-PBF processing. Melt pool boundaries are marked orange a) Dendritic solidification in AlSi10Mg alloy with different cooling rates (G_L.R) at the boundary of meltpools depicted with different dendrite arm spacing (inset) b) Cellular solidification marked in yellow in Al-Mn-Cr-Zr alloy showing Al-Mn precipitates aligned along the solidification structure boundary (inset).

2.3 Aluminium Alloys

Aluminium (Al) is the most abundant metal in the earth's crust and is one of the most mined metals [37]. It can be recycled completely, thus making it lucrative for achieving sustainability goals with full circularity being possible. The low density and high alloying capability of aluminium make it useful in a wide variety of applications, from cheap light-weight shelves to expensive aerospace structures [8]. Aluminium can be conventionally manufactured using casting or be shaped into products from wrought material. The alloy grades are usually defined by the major alloying elements and the common grades include the 1xxx,2xxx... 7xxx series. There are also novel alloys like the Al-Li alloys. It is common to distinguish between wrought and cast alloys as this irrespective of the manufacturing route used for some series of alloy. Also, the alloys are divided into non-heat treatable alloys and heat treatable alloys, where the latter can achieve higher strengths with precipitation hardening. Typical examples of Al-alloys are medium-high strength 6xxx series aluminium alloys which are age hardened using Mg_2Si precipitates, with 6061/ 6082 being famous grades of this series of alloys [38]. Pure aluminium has low yield strength (15 MPa), but the alloying and precipitation hardening can bring the yield strength up to 500-600 MPa.

The alloying of aluminium could hence be done with scope of implementing solid solution strengthening (with typical elements such as Mg, Mn, Cu), precipitation strengthening (with typical precipitates Mg_2Si or $MgZn_2$) and to some extent grain size strengthening (also called Hall-Petch effect). To this comes also the aforementioned strain hardening that is applied in the case of wrought alloys. The solid solution strengthening of aluminium generally focuses on substitutional solid solutions, with alloying elements replacing the aluminium atoms, thus creating a stress field around each such atom due to a different atomic radius as shown in Figure 8. Such a stress field (also represented as lattice misfit strain) helps in strengthening the whole matrix by restricting the dislocation motion.

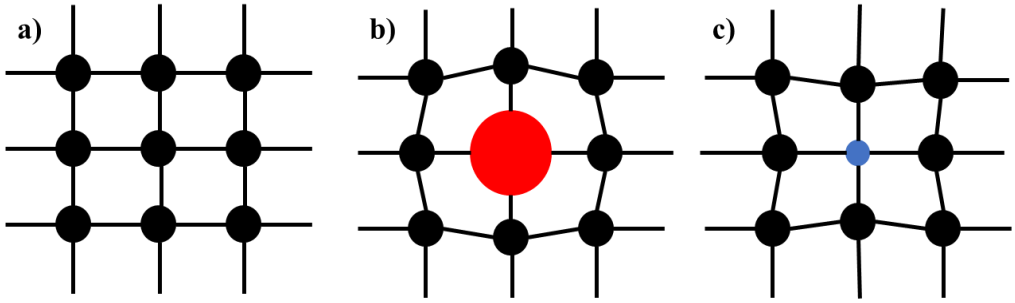

Figure 8 Solid solution strengthening for substitutional elements, where black dots represent Al-matrix, red and blue dots represent atoms of larger and smaller atomic size respectively. Larger atoms apply a positive strain to the matrix whereas smaller atoms apply a negative strain to the matrix.

The solid solution strengthening increases the yield strength following Equation 2 [39, 40].

$$\Delta\boldsymbol{\sigma_{YS}} \propto \boldsymbol{c}^{\frac{2}{3}}.\left|\boldsymbol{\varepsilon}^{\frac{4}{3}}\right| \tag{2}$$

The parameters in the equations above are as follows.

$\Delta\boldsymbol{\sigma_{YS}}$	=	Increase in yield strength (MPa)
$\boldsymbol{c}$	=	Concentration of element in Al-matrix (at%)
$\boldsymbol{\varepsilon}$	=	Lattice misfit strain (%)

Furthermore, strengthening may be achieved via precipitation strengthening or precipitation hardening. Usually, some precipitates are formed during solidification due to elemental segregation at slow cooling conditions in conventional manufacturing. Thus, the alloy must then be first solution heat treated just below the solidus temperature to dissolve such low melting precipitates [41, 42]. Let's consider the Al-Cu binary alloy as a prototype example for the solutioning and subsequent precipitation hardening. As shown in Figure 9 a) for Al-Cu alloy, up to 5.6 wt% Cu can be dissolved by solution heat treatment of up to 800-810 K. The solution heat treatment is followed by quenching in water. Subsequently, Cu present in the solid solution reacts with Al forming secondary phase precipitates with the ultimate development of the equilibrium phase precipitates of composition Al_2Cu, as the alloy is subjected to precipitation treatment temperatures (400-500 K). Initially, there is formation of very small precursors called Guinier-Preston zones (GP Zones). These clusters are several angstrom (Å) in size, adopting disc shaped morphology with the faces of the disc being fully coherent with Al-matrix. Although the formation of these precipitates is associated with increase in Gibbs free energy, as shown schematically in Figure 9 b), their coherence with the Al-matrix reduces the activation energy barriers significantly, thus favouring their formation kinetically during heat treatments. Upon ageing for some time, there is growth of the clusters, whereby the coherency with the matrix is lost and transformation to more stable precipitates take place following the sequence Θ''→Θ'→Θ (nomenclature discussed in Table 1); the reason being that these phases have a lower Gibbs energy values [43, 44]. The Θ phase is the most stable form and its precipitates are incoherent with the Al-matrix, and it does not impart as high hardness to the matrix as Θ'' or Θ' precipitates. Due to its incoherence with the Al-matrix, the Θ phase can be detrimental to the ductility of the Al-matrix as it adds coherency stresses to the matrix. Thus, the ageing treatment in the Al-Cu system is defined by controlling the size of precipitates in order to achieve highest volume fraction and sizes of Θ'' or Θ' precipitates while preventing stabilisation to Θ, to provide

the best strength to the matrix. It can also be seen in Figure 9 c) how ThermoCalc simulations can be applied to predict the sequence of formation of the aforementioned phases. This simulation can be quite useful when developing heat treatments for novel alloys as the tentative time and temperatures for such treatments can then be depicted with fewer experiments to optimise the size and volume fraction of desirable precipitates. The precipitation sequence for some Al-alloys is shown in Table 1 which depicts a similar sequence as explained before. In Al-alloys manufactured via AM, this sequence may be different as shown by [45, 46], wherein a AlSi10Mg alloy was processed via LB-PBF. During in-situ TEM coupled with XRD and DSC techniques, clusters similar to the GP Zones were seen as Si-clusters in as-printed samples. However, upon heat treatment, the β family precipitates or their precursors were not seen in either of the two studies, whereas Al-Si precipitates were observed instead.

Table 1 Precipitation sequence for conventionally manufactured Al-alloys [43]

Alloy	Precipitation sequence
Al-Ag	GPZ (spheres) → ɣ' (plates) → ɣ (Ag_2Al)
Al-Cu	GPZ (discs) → Θ'' (discs) → Θ' (plates) → Θ ($CuAl_2$)
Al-Cu-Mg	GPZ (rods) → S' (laths) → S ($CuMgAl_2$) (laths)
Al-Zn-Mg	GPZ (spheres) → η' (plates) → η ($MgZn_2$) (plates or rods)
Al-Mg-Si	GPZ (rods) → β' (rods) → β (Mg_2Si) (plates)

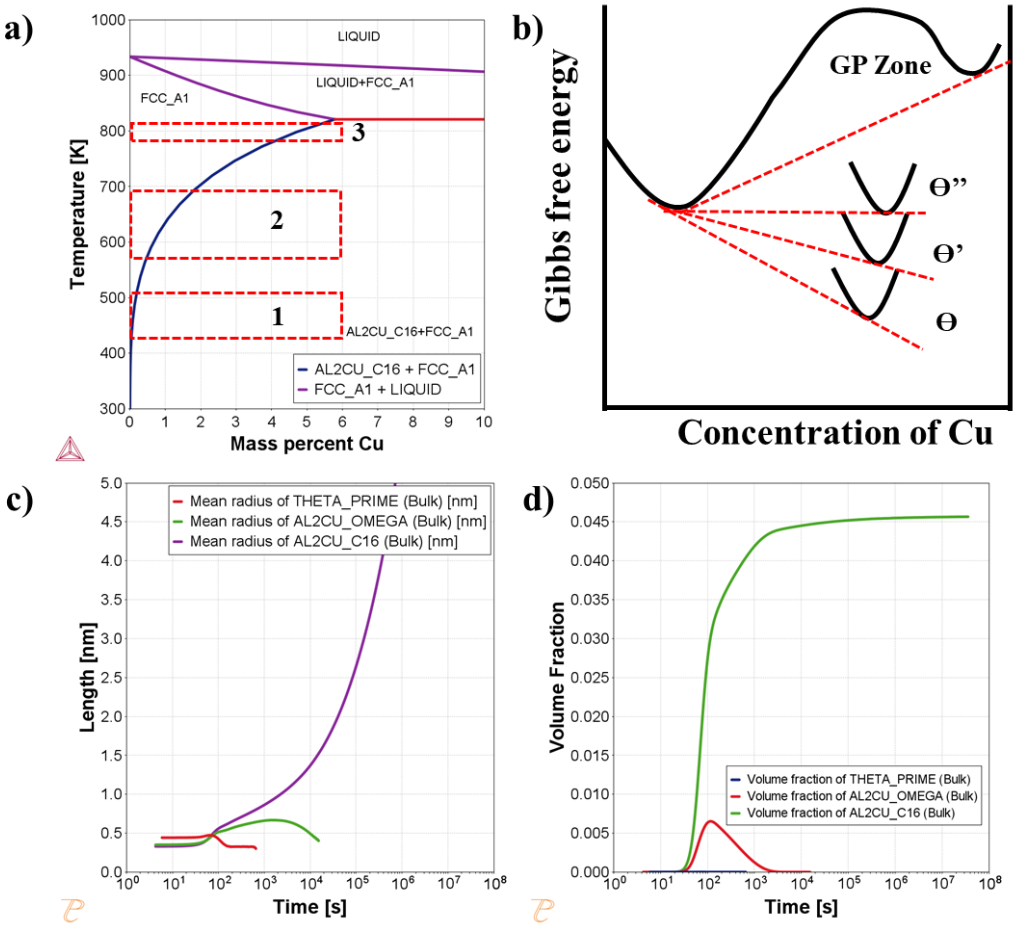

Figure 9 a) Equilibrium phase diagram for Al-Cu binary system with region 1,2,3 representing zones for precipitation treatment, annealing and solution heat treatment respectively [41]. Phase diagram drawn using ThermoCalc 2021a b) Schematic molar free energy diagram for Al-Cu system showing the Gibbs free energy for various Al-Cu phases, adapted from [43] c),d) Isothermal precipitation in Al-4wt%Cu at 473 K simulated using PRISMA module in ThermoCalc 2021a with TCAL7, MOBAL5 databases showing mean radius (nm) and volume fraction respectively. Theta_prime is Θ'', Al2Cu_Omega is Θ' while Al2Cu_C16 is Θ phase in a). GP Zones could not be simulated in this simulation.

After identifying the precipitate type, the modus operandi of hardening for these precipitates needs to be identified. In aluminium alloys, the hardening precipitates impart strength mainly via a balance between shearing mechanisms and Orowan looping mechanisms. Shearing mechanism was defined by Nembach [47] and supposed to exist when precipitates are very small (nominal size of <10-20 nm). For such conditions, the dislocations can shear the precipitates and thus strengthening comes from the shear modulus difference between matrix and precipitate. As the precipitates grow, a potentially weaker mechanism called Orowan looping takes place [48]; here the dislocation movement must loop around a precipitate to move in the crystal lattice. Both the mechanisms are illustrated for simple spherical shaped precipitates in 2D-view model in Figure 10.

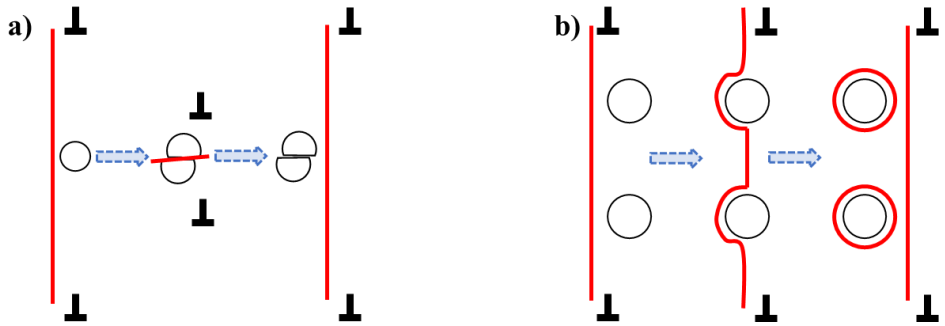

Figure 10 a) Dislocation movement leading to shearing of precipitates (shear hardening mechanism) b)Dislocation movement leading to looping around the precipitates (Orowan looping mechanism)

Nembach's shear hardnening mechanism can be represented by Equation 3 [47, 49].

$$\Delta\sigma_{YS} = \mathbf{0.0055}.M.(\Delta G)^{\frac{3}{2}}.\left(\frac{2.f_v}{G}\right)^{\frac{1}{2}}.\left(\frac{R}{b}\right)^{\left(\frac{3m}{2}-1\right)} \quad (3)$$

Orowan looping mechanism can be represented by the Orowan-Ashby formula in Equation 4 [48].

$$\Delta\sigma_{YS} = \frac{0.13.G.b}{2.R.\left(\left(\frac{1}{2.f_v}\right)^{\frac{1}{2}}-1\right)}.ln\left(\frac{R}{b}\right) \quad (4)$$

The parameters in the equations above are as follows.

$\Delta\sigma_{YS}$	=	Increase in yield strength (MPa)
M	=	Taylor's mean orientation factor= 3.06 [50]
ΔG	=	Difference in shear modulus between the precipitate and Al-matrix
f_v	=	Volume fraction of precipitates
G	=	Shear modulus of pure Al
R	=	Radius of precipitates (nm)
b	=	Burger's vector of Al = 0.286 nm [51]
m	=	Material dependent constant = 0.85 [49]

It can be summarized that at constant volume fraction of precipitates, the shear mechanism increases strength with precipitate size. On the other hand, the Orowan looping mechanism decreases strength with precipitate size, as illustrated in Figure 11. The strengthening by a precipitate is defined by the weaker mechanism of the two at given size, as failure occurs at the weakest site. Thus, there exists a critical radius r_c, at which the benefits from the mechanisms meet and a maximum hardening effect is achieved (denoted as σ_{peak} in Figure 11). Heat treatments for precipitation hardening for Al-alloys intend to achieve this peak hardening (σ_{peak}) to get maximum strength.

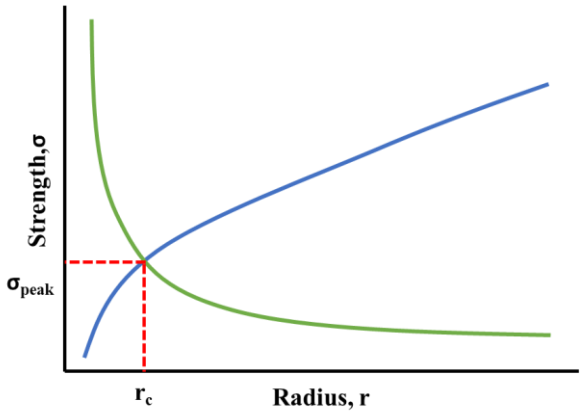

Figure 11 Typical precipitation strengthening mechanisms represented as plot of strength and precipitate radius. Shear hardening mechanism (blue) has proportional relationship between strength and precipitate radius, whereas Orowan looping mechanism (green) has an inverse relationship between strength and precipitate radius. The highest strength (σ_{peak}) is achieved where the two curves intersect.

Grain size refinement effect, better known as the Hall-Petch effect [52, 53, 54] refers to an increase in yield strength inversely proportional to the grain size of the material. Typically, it can be shown in Equation 5.

$$\boldsymbol{\sigma_{YS}} = \boldsymbol{\sigma_o} + \boldsymbol{k}.\frac{\mathbf{1}}{\sqrt{\boldsymbol{D}}} \tag{5}$$

The parameters in the equation above are as follows.

$\boldsymbol{\sigma_{YS}}$	=	Increase in Yield Strength (MPa)
$\boldsymbol{\sigma_o}$	=	Initial strength of material (MPa)
$\boldsymbol{k}$	=	Chemistry and microstructure dependent constant
$\boldsymbol{D}$	=	Grain size

This effect is usually a powerful mechanism to strengthen alloys such as Fe-based or Ni-based. However, this effect is significantly weaker in Al-based alloys as the constant k is 1/3 value as that of Fe-based alloys [52]. Taking the Hall-Petch factors from [52] as basis for comparison, examples for three different families of alloys and three different grain sizes in Table 2. It has been shown that the increase in yield strength going from 100 µm → 1 µm grain size in Fe-based alloys yields ~212 MPa increase in strength whereas it only yields ~61.5 MPa increase for Al-based alloys.

Table 2 Hall-Petch effect on different families of alloys. Three different grain sizes are considered for three families of alloys and the increase in yield strength is calculated as difference in yield strength from base value (100 µm grain size) [52]

Material family	Hall-Petch constant (k) MPa. µm$^{1/2}$	Grain size (in µm)	Increase in yield strength (MPa)
Fe-based	310	100	0
		10	67
		1	212
Ni-based	230	100	0
		10	50
		1	157
Al-based	90	100	0
		10	19.5
		1	61.5

Therefore, it can be considered that for Al-alloys, all three mechanisms contribute to strengthening, but with precipitation strengthening being the main contributor. Strain hardening could also be induced by cold forming operations, which could produce strengthening due to plasticising the material beyond elastic limit. This effect is weak in case of Al-alloys, as discussed in [55]. Moreover, in context of

additive manufacturing, it does not seem viable to apply a cold forming operation even if it is a method used for conventional materials.

Besides its high specific strength, aluminium is also famous for high thermal and electrical conductivity along with corrosion resistance due to formation of passive Al_2O_3 layer on the surface. This oxide layer is stable as long as the environment is not too acidic or alkaline, i.e., in the pH range of 4-9 [56]. This makes the application of aluminium advantageous in electrification components, heat exchangers and even in medium aggressive corrosive environments.

2.4 Calculation of Phase Diagrams Approach to Alloy Design

Calculation of phase diagrams (CALPHAD) was a technique developed by Larry Kaufman about 50 years ago. According to [57], it is a reliable method of predicting thermodynamics, kinetics, and other properties of multicomponent material systems. This helps to combine available data on known material system and utilise them along with thermodynamically driven systems to develop future materials. For aluminium alloys, such techniques have been shown to be successful in developing the effects of alloying elements in solid solution and effects of precipitate formation on strengthening by several researchers [58, 59, 60]. Over the years, the methodology has proven to be quite useful in developing new alloys or predicting the properties of available alloys. ThermoCalc AB, which was started at KTH University in Sweden is a company that develops such software for CALPHAD and related techniques. For this research study, ThermoCalc software was used as an anchoring point when calculating aspects of alloy design for LB-PBF.

It was realised that ThermoCalc software, can sometimes miss out on predicting the processing conditions formed during rapid solidification and remelting obtained in LB-PBF. As shown in Figure 5, LP-PBF processed materials show a complex thermal history which cannot be accounted for when doing solidification simulations using ThermoCalc. Consequently, ThermoCalc was used as an indicator, rather than a definitive tool for prediction of phases that in turn end up in intended microstructure and properties.

2.5 Integrated Computational Materials Engineering

Integrated computational materials engineering (ICME) is a relatively new field of study which promises to revolutionise the way components are designed. This is done by understanding a material's processing-structure-property-performance relationship and by applying advanced tools such as CALPHAD or machine learning approaches to design new materials suitable for the desired application with significant reduction in time and cost [61, 62, 63]. Such methods rely on modern computing capabilities to predict microstructures and resulting properties from fundamental thermodynamic principles combined with available historical metallurgical data. This also provides a framework for quicker material design suitable for novel processing routes as well (albeit with some modifications). An illustration for a typical processing-structure-property-performance relationship for an AM material is shown in Figure 12. It has been adapted to show how the direct/ indirect relationship between different process conditions can lead to different structures and resulting properties. This plays an important role as a feedback loop to alloy design, but at the same time it can be a great tool to develop advanced alloys rapidly with extensive knowledge of these process-structure-property relations, in order to tailor alloy design. An example is shown in Figure 13, where two Ashby charts drawn in GRANTA Edupack 2021. Here typically high strength Al-alloys (age hardenable Al-alloys) have average performance when plotted against a secondary property such as high young's modulus or higher maximum service temperature. Thus, applications requiring secondary properties (such as high maximum service temperature of 200 ºC/ 473 K) will have to rely on inherently weaker cast Al-alloys with about 250-300 MPa strength instead of about 500-550 MPa. This implies that the relative strengthening mechanisms for precipitation need to be analysed if higher strength properties are desirable at higher temperatures;

this requires new chemistries where precipitates do not develop quickly and may stay stable at elevated temperatures [64]. In this way, ICME as a tool could help advance alloy design to find these "empty spaces" where new alloys are required for advanced applications and develop such high-performance alloys. One great example is the new Al-Ni based cast alloy develop for Tesla Motor's electric vehicles, allowing the application of large die casting components without hot tearing and still retaining 45-50% conductivity (with respect to IACS or International Annealed Copper Standard) [65].

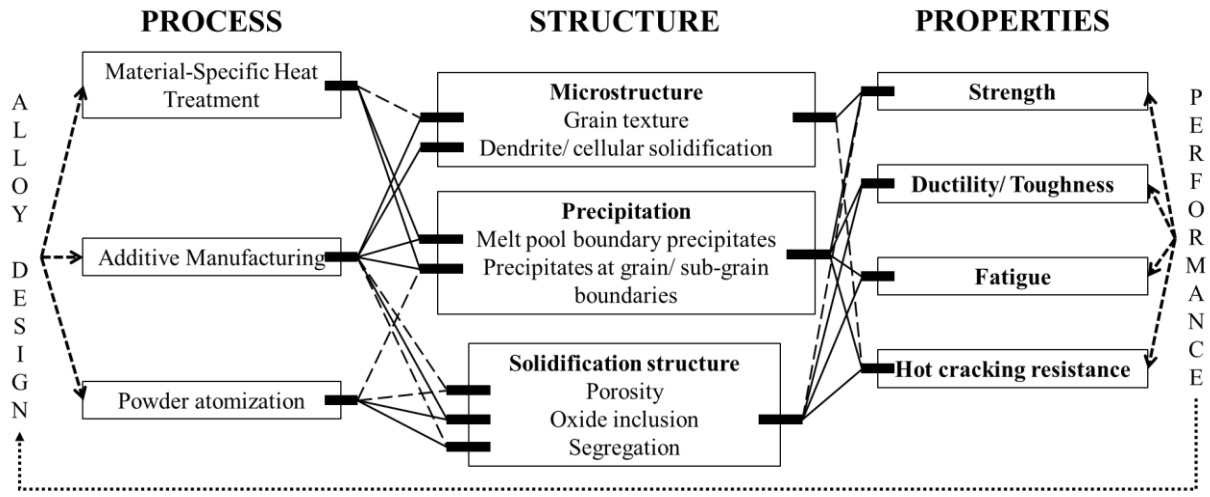

Figure 12 Typical processing-structure-property-performance relationship for an AM material. Adapted from [66]

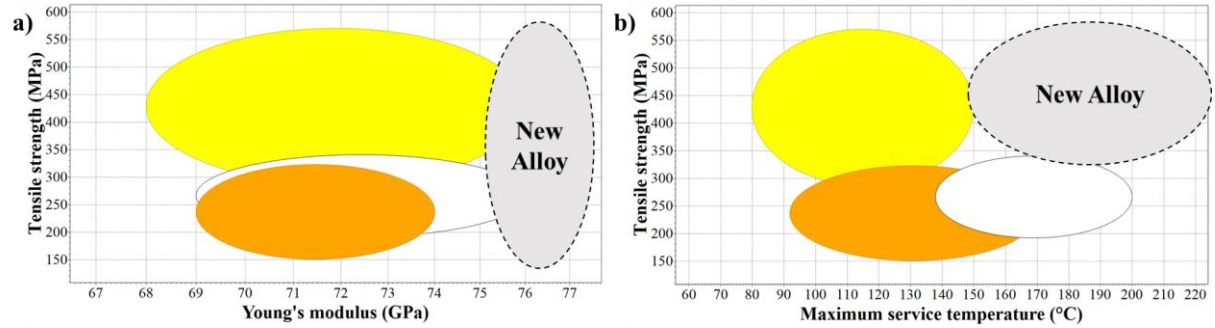

Figure 13 Ashby charts showing typical performance of Al-alloys. Age-hardenable wrought Al-alloys (yellow) have highest tensile strengths (MPa) followed by cast Al-alloys(white) and non-age-hardenable Al-alloys (orange). Possible area for new Al-alloys is marked in grey a) Youngs's modulus (GPa) vs Tensile strength (MPa) and b) Maximum service temperature (°C) vs Tensile strength (MPa).

2.6 Tailored Alloy Design for LB-PBF

This section will discuss tailored alloy design that can be brought into use in LB-PBF. By combining the available thermodynamic information for a certain alloy system with knowledge of LB-PBF process, novel compositions can be designed while handling issues such as solidification cracking. At the same time, since the processing condition for LB-PBF is understood, a higher supersaturation of special elements can be depicted, which in turn means that precipitation can be set in a favourable way during subsequent heat treatments.

2.6.1 Solidification Cracking: Causes and Countermeasures

Aluminium alloys are affected by solidification issues such as solidification cracking. As explained classically by [11], this cracking occurs when solidification is near completion (fraction of solid, f_s ~ 0.8-1). During solidification, aluminium grains may have a larger solidification range, which arises from a segregation of elements into the last liquid. This leads to difference in thermal expansion

coefficients between liquid and solid aluminium. Two adjacent Al-grains under stress are thus left with a thin channel to fill and very little time for the melt to fill it up. This causes columnar cracks at intergranular boundaries. This issue is also common in welding of metals [13]. Thus, most of the commercial alloys available for LB-PBF are easily weldable alloys, AlSi10Mg and 316L stainless steels being great examples. Two solutions for avoiding solidification cracking are considered as examples in this section. The first example shows segregation potential of certain elements upon solidification in Al-system. This is shown in Figure 14, where Al-Mg binary system is compared with Al-Mn binary system. The compositions are varied between 0-5 wt% of each alloying element, with an increment of 1 wt% along the red dotted line. Adding Mg to the system will significantly increase the solidification range to up to 200 K at 5 wt% Mg as compared to 0 K in 0 wt% Mg (pure Al). This can lead to solidification cracks as Mg would segregate and be enriched in the liquid aluminium close to complete solidification, thus causing solidification cracking along grain boundaries. On the other hand, Mn forms precipitates early on during the reaction which are of Al_4Mn or Al_6Mn stoichiometry; there are no relative segregations later in the solidification range and enrichment in the liquid close to complete solidification, thus keeping the solidification range ~0 K. This means that there is a general low susceptibility to solidification cracking when using Mn rather than Mg.

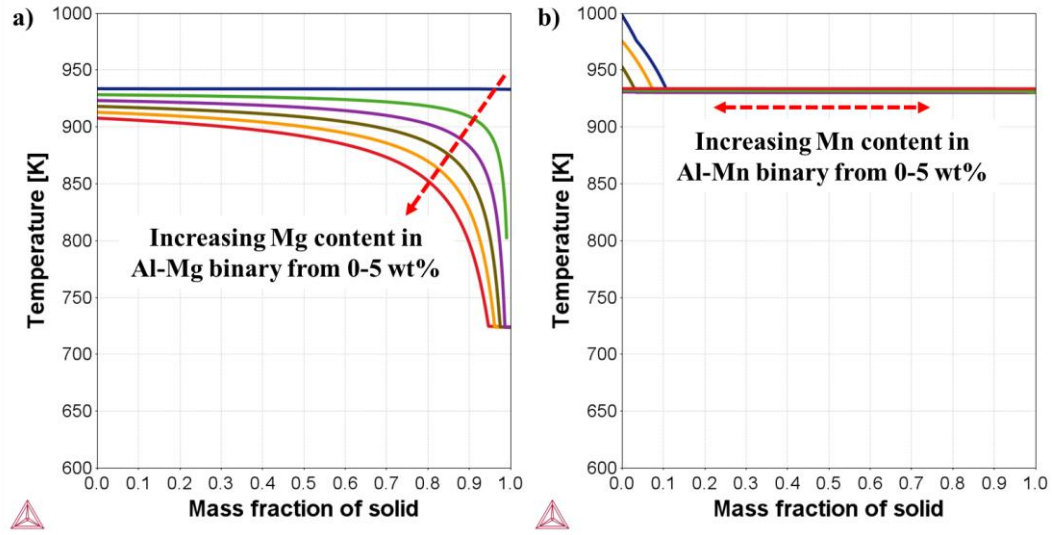

Figure 14 a) Scheil solidification curve for Al-Mg binary alloy from 0-5wt% Mg in 1wt% increments b) Scheil solidification curve for Al-Mn binary alloy from 0-5wt% Mn in 1wt% increments. The calculations have been done using ThermoCalc 2021a with TCAL7 database. It is seen that increasing Mg content increases the solidification range significantly from 0→~200K; however, it stays relatively constant by changing Mn content, suggesting little segregations close to solidification.

As mentioned before, local shrinkage effect caused by segregation could result in solidification cracking. An alternative path to reduce cracking could be relaxation of stresses by formation of equiaxed Al-grains nucleating on pre-existing primary precipitates in the melt; the primary precipitates may act as nucleation sites, which could make Al-Mg containing alloys printable. In this way, the issue causing solidification cracking is counteracted. This was the concept behind the second solution to solidification cracking, as shown in the famous Scalmalloy®, which is an Al-Mg-Sc-Zr alloy. In this alloy system, 4.5-5 wt% Mg is used, and high densities are reported [67, 17]. This was made possible with $Al_3(Sc,Zr)$ primary cubic precipitates acting as nucleants to nucleate equiaxed Al-grains during solidification. Secondly, 7075-series aluminium alloy was also shown to be printable with high densities [12]. These alloys, which usually consists of 2.1-2.9 wt% Mg and 5.1-6.1 wt% Zn making them unprintable. However, this was resolved by coating the Al-powder by ZrH_2 which is a semi-stable form of Zr that breaks down to primary Al_3Zr during LB-PBF processing, and causes grain refinement, analogous to Scalmalloy®. These solutions are currently not possible to be embedded in Scheil solidification due to the assumption of the system that once the primary precipitates form, they do not react with the liquid

metal. Additionally, the liquid & surfaces of the solid phases are in equilibrium, which makes the positive impact of $Al_3(Sc,Zr)$ hard to simulate [68].

2.6.2 Higher Supersaturation due to LB-PBF

Another major aspect of tailored alloy design is the achievement of high supersaturation in LB-PBF. During LB-PBF high cooling rates are achieved. This means that a proportional high supersaturation of the matrix can be expected, further away from equilibrium solubility than in a cast material. For Al-alloys, it was found out that transition series elements with low solubility in cast-Al are interesting. As shown in Figure 15 a), the solid solubility of transition elements is increased by few orders of magnitude by raising cooling rates in binary Al-alloys to 10^5-10^6 K/s [69]. This means that such a concept can lead to formation of entirely new families of aluminium alloys with these elements in supersaturated solid. Secondly, Figure 15 b) shows the bulk diffusivities of these transition elements in Al-matrix at high temperatures with respect to common alloying elements like Mg, Cu and Si. Since the diffusion coefficient of many of the transition elements is several orders of magnitude lower than Mg, Cu and Si, this would mean that nucleation and growth kinetics of secondary precipitates formed during remelting in LB-PBF processing, or during later heat treatments would be severely retarded due to slower diffusion of elements.

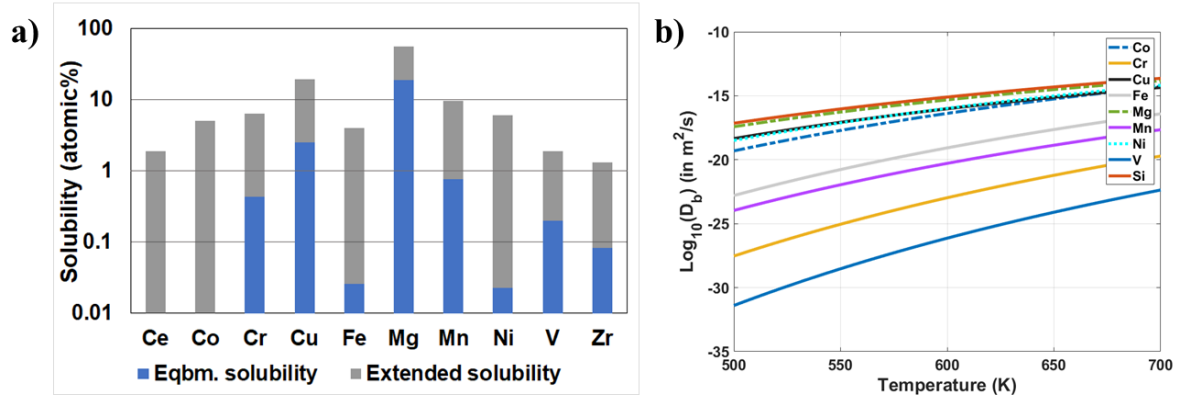

Figure 15 a) Extension of equilibrium solubility achieved in binary Al-alloys at high cooling rates (up to 10^6 K/s) [69] b) Bulk diffusivities of various elements in solid Al at higher temperatures (500-700 K). Calculated from [70]

The higher dissolution of solutes can also be illustrated using ThermoCalc-predicted phase diagrams, as shown in Figure 16. It is seen in the Al-Zr binary diagram that Zr forms a primary precipitate during solidification at very high temperatures (>1000K). A peritectic point at 0.25 wt% Zr exists, which demarcates the limit of solubility of Zr in Al matrix. However, if the formation of the stable Al3ZR_D023 (the stable orthorhombic Al_3Zr phase) is suppressed, the peritectic point shifts towards the right, i.e., higher Zr content, thus dissolving 0.5 wt% Zr, increasing the Zr solubility limit by approximately two times and forming the Al3X (the metastable cubic Al_3Zr phase) instead. In the ThermoCalc software this can be applied by suppressing a certain stable phase. Hence the chemical reaction proceeds by lowering the Gibbs free energy of the system without that suppressed phase. Since the other phase (metastable Al3X) is associated with different properties such as Gibbs free energy of formation, all the solvus lines move accordingly. Experimentally, it has been shown by several authors that metastable Al_3Zr phases are formed (similar to Al3X in ThermoCalc), which are responsible for grain refinement. Also, the limit of Zr solubility in LB-PBF systems has been shown to be 0.6-0.7 wt% experimentally, thus confirming the validity of such a method to some extent [18, 71].

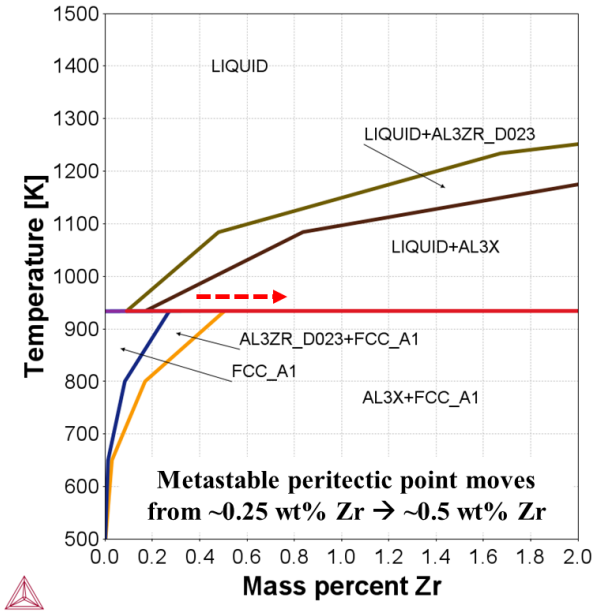

Figure 16 Phase diagram for Al-Zr system showing that if the stable Al_3Zr phase (Al3ZR_D023) is suppressed, a metastable equilibrium curve can be shown with Al3X as a phase, which is the metastable Al_3Zr phase. This type of calculation also sheds light on the shift of peritectic point from ~0.25wt% Zr to ~0.5wt% Zr, which means higher Zr could be dissolvable in solid solution at rapid cooling rates.

The only limitation of assuming higher supersaturation is to be aware of remelting during LB-PBF process, as illustrated in Figure 5. This remelted region could then be susceptible to precipitate formation as indicated as Al_6Mn precipitates forming in beginning of solidification in Figure 14 b). This could lead to decrease in maximum supersaturation possible through LB-PBF and consequently, the alloy design may need to account for such remelting effects.

2.6.3 Selection of Alloying Elements Coupled with Expected Alloy Application

Based on previous examples, several known and unknown alloying systems with preferably containing transition series elements were validated. Some other factors affecting the choice of alloying elements was to avoid use of certain elements. Such elements could have been avoided due to high cost (such as Sc) or due to their mining in conflict regions (such as Co) [72, 73]. This approach is ideal as it allows for the development of alloys that are sustainable (in terms of reduced cost and raw material availability) and viable for industrial applications, rather than optimising only for strength.

After a thorough literature study and patent search, it was decided to use Mn, Cr and Zr (with possibility to add Mg later) as a possible alloying system. As seen in Figure 15 b), Mn and Cr were the slowest diffusing elements after Vanadium (V). Also, Al-alloy systems involving Mn and Cr were studied in 1980s-1990s to develop materials for manufacturing via powder metallurgy route with good results [74, 75]. It was seen that their solid solution effect was strong with an age hardening response. Additionally, Cr was seen to stabilise the hardening $Al_{12}Mn$ precipitate. The element Zr was considered instead of Sc due to sheer cost difference compared to that of Sc. Additionally, Zr diffuses slower than Sc, giving a better chance to control precipitate growth at higher temperatures. Choosing the indicated elements was believed to create an alloy system expected to have medium-high strengths coupled with high temperature properties. The high temperature applications for aluminium alloys are immense in aerospace and automotive industries [64, 76]. And as shown in Figure 13 b), there is a gap in Ashby chart for high strength, high temperature alloys, thus highlighting the need for this particular family of alloys.

Chapter 3 – Experimental Methods

3.1 Materials

The different material families discussed as a part of this thesis study are described in the following sections.

3.1.1 Al-Mn-Cr-Zr Family

This is a new family of aluminium alloys developed as a part of this research work. It has been developed in close collaboration with Höganäs AB who have applied for a patent for this (application number EP20212934). The family is developed as a proof of concept showing extended supersaturation limits achieved using LB-PBF (up to 7 wt% Mn + Cr in solid solution). Further, four variants of the alloy family, as shown in Table 3 are discussed in this thesis study. Table 3 also shows the actual chemical compositions of the powder variants in their as-received condition and those of the printed samples, conducted using ICP-AES technique.

Table 3 Alloy compositions for Al-Mn-Cr-Zr alloys in as-atomised and as-printed condition, measured using ICP-AES technique. All the alloys had 0.16-0.17 wt% Fe, Si each as impurities from atomisation process.

Alloy name	Alloy composition (as-designed, wt%)	Alloy composition (as-atomised, wt %)	Alloy composition (as-printed, wt%)
Alloy A	Al 4.75Mn 1.25Zr	Al 4.7Mn 0.48Zr	Al 4.8Mn 0.47Zr
Alloy B	Al 4.75Mn 0.75Cr	Al 5.0Mn 0.80Cr	Al 4.9Mn 0.80Cr
Alloy C1	Al 4.75Mn 0.75Cr 0.7Zr	Al 4.9Mn 0.80Cr 0.56Zr	Al 4.9Mn 0.80Cr 0.56Zr
Alloy C2	Al 4.75Mn 0.75Cr 1.25Zr	Al 5.0Mn 0.80Cr 0.59Zr	Al 5.0Mn 0.80Cr 0.60Zr

The particle size distribution of the four powder variants was designed to be between 20-53 µm; the actual values in terms of D10, D50 and D90 are summarized in Table 4 and Figure 17. The test was conducted on a Mastersizer 3000 laser diffraction machine from Malvern, UK. The values were averaged over five measurements.

Table 4 Particle size distribution for Al-Mn-Cr-Zr alloys

Sample Name	D10 (µm)	D50 (µm)	D90 (µm)
Alloy A	18.5	29.1	46.7
Alloy B	20.4	33.4	56.1
Alloy C1	19.0	30.5	51.0
Alloy C2	18.1	28.7	47.0

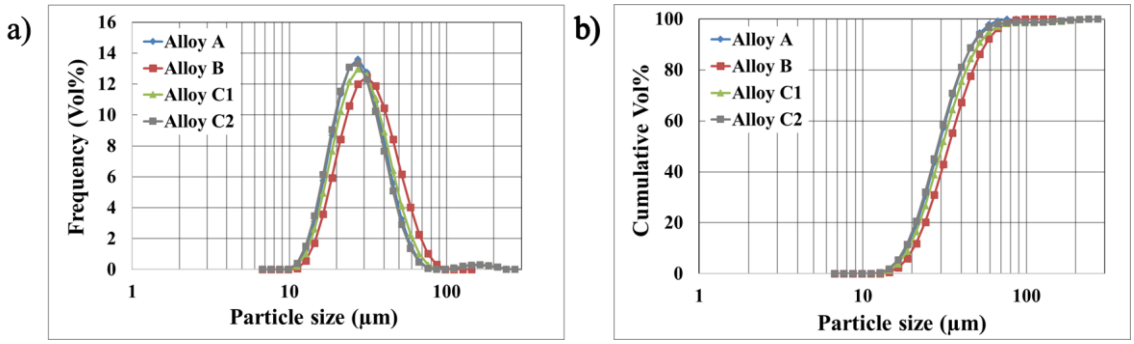

Figure 17 a) Particle size (µm) vs volume% and b) Particle size (µm) vs cumulative volume%

3.1.2 Al-Mg-Sc-Zr Family (Scalmalloy®)

The Scalmalloy® powder was provided by Höganäs AB. The powder was gas-atomized to a bit coarser specification than powder of the Al-Mn-Cr-Zr alloys. It was seen that the D90 value for this alloy was

close to 70 µm as compared to 50 µm (average of four alloys) in case of powder of the Al-Mn-Cr-Zr alloys. The chemical composition and particle size distribution of the Scalmalloy® powder as well as the composition after printing are summarised in Figure 18 and Table 5. Similar procedure and same equipment were used for testing this powder as in the case of Al-Mn-Cr-Zr family of alloys.

Table 5 Summary of chemical composition (wt%) for Scalmalloy® powder, measured using ICP-AES technique at Höganäs AB. All the alloys had 0.12 wt% Fe, 0.06 wt% Si as impurities from atomisation process. The powder size distribution for the alloy is also shown in µm

Powder Chemistry	As-atomised, wt%	Al 4.7Mg 0.7Sc 0.27Zr 0.48Mn
	As-printed, wt%	Al 4.3Mg 0.7Sc 0.27Zr 0.48Mn
Powder size distribution	D10 (µm)	34.1
	D50 (µm)	48.6
	D90 (µm)	68.9

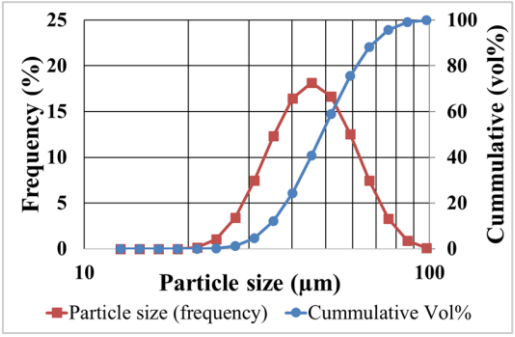

Figure 18 a) Particle size (µm) vs volume% and cumulative volume % respectively for Scalmalloy® powder

3.2 LB-PBF Processing

All the five alloys were printed using an EOS M100 LB-PBF machine (from EOS GmbH, Germany), equipped with Yb-fibre laser having spot size of 40 µm and maximum power of 200 W (170 W nominal). It is worth mentioning that this machine was not developed for Al-alloys, as the interest in LB-PBF processing of aluminium usually have requirements for larger components than the build volume of the machine in question can provide (cylindrical dimensions: 100 mm diameter x 100 mm height). Hence, there were no "standard" processing parameters for the machine that could be used. These parameters were developed following a simple two-factorial design of experiment approach by having two variables for achieving high relative density (>99%). The samples were printed following a constant power and layer thickness of 170 W and 0.03 mm respectively. The laser scan speed and hatch distance were then varied, as shown in Figure 19, to develop a two-dimensional surface plot and thus to conceive the processing conditions providing high-density results.

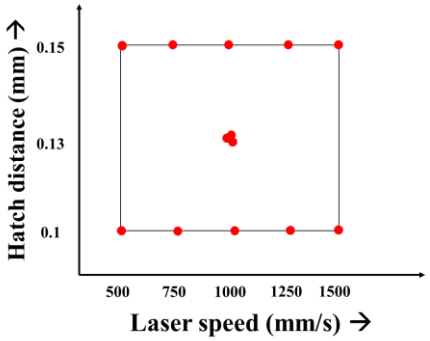

Figure 19 Two-factorial design of experiment utilized for achieving processing window in EOS M100 machine. Red spots demarcate the processing parameters selected.

Subsequently, the printing for one of the Al-Mn-Cr-Zr alloys (alloy C2) was further investigated by varying the laser power between 100-170 W as a third variable to develop a three-dimensional processing window with laser power, laser scan speed and hatch distance as the three variables.

3.3 Sample Preparation

All the samples that were LB-PBF processed were cut from the build plate using a cold saw. Two different sizes of samples were designed:

1. Cubes of 10 mm x 10 mm x 10 mm for design of experiment tests
2. Cuboids of 8 mm x 8 mm x 16 mm for further testing such as heat treatments, microscopy etc. The reason for choosing smaller dimensions was to fit a higher number of samples in single build job.

The sample design is shown in Figure 20. Denotations X and Y refer to the coordinates in the build plane, while Z represents the build direction. The samples were designed with notches to mark the gas flow direction (X) during printing and to provide markers for microscopy analysis. The intention of doing the preparation and investigation this way was to rule out (if any) effects of gas flow on relative density of the samples during printing. Approximate cutting planes used for each sample are also shown. Samples for design of experiment tests were cut along three planes XZ, XY and YZ whereas the other samples for heat treatment, microscopy etc. were cut along XY and XZ direction only.

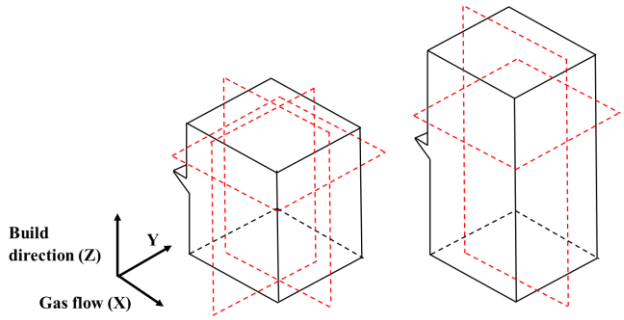

Figure 20 Two types of samples printed. Left: 10mmx10mmx10mm cube and right: 8mmx8mmx16mm cuboid. The red lines mark the approximate cutting planes used while doing sample preparation. The samples were having a notch along the X direction, to mark the Ar gas flow during printing.

After cutting, all the samples were mounted on a conductive resin called Polyfast (from Struers). The sample grinding/ polishing step was developed from Struers standard procedure for Al-Si cast alloys [77]. It was seen that LB-PBF materials were harder to get consistently good samples without scratches, so a self-developed procedure was developed by adding more steps and varying loads. The samples were grinded till flat and later polished for further analysis. The grinding and polishing steps are shown in Table 6. All the samples were kept in ultrasonicator machine dipped in water between all the steps till 1 µm polishing for 4-5 minutes each to remove loose powder or resin stuck to the samples. This method consumed considerably longer time than usual Struers methods, but the results were seen to be consistent, and scratch free samples were achieved.

Table 6 Grinding and polishing steps used for all five Al alloys. Samples for optical microscopy were only polished till 1µm. The samples for electron microscopy were polished with OP-S/OP-U suspensions

Procedure	Foil/ Polishing cloth used	Time (min)/ Force (N)
Grinding	240 Si foil	2-3 min/ 25 N
	500 Si foil	3-4 min/ 25 N
	1000/1200 Si foil	5 min/ 25 N
	2000 Si foil	5-6 min/ 20 N
	4000 Si foil	6-8 min/ 20 N
Polishing	MD-Nap cloth (1µm diamond paste)	5-6 min/ 20 N, 5-6min/ 15N
	MD-chem cloth (OP-S/OP-U suspension)	1-2 min/ 10 N (with suspension), 2 min/ 10 N (water wash)

Etching of the Al-samples was avoided as most of the samples were tested using back scattered mode in electron microscopy with good results. Few samples were etched to see to see the segregation of precipitates at different areas of a sample when observed under optical microscope. The etchant used was Keller's reagent (90 mL water, 2.5 mL HNO_3, 1.5 mL HCl and 1 mL HF) and etching was done by dipping a freshly polished sample in this reagent for 8-10 s and then directly dip the sample in water to neutralise the effect of the reagent. The samples were then immediately cleaned with ethanol and dried to be subsequently used for microscopy.

3.4 Analysis Techniques

3.4.1 CALPHAD Simulation and Precipitation Modelling

The calculations conducted for alloy modelling and simulation of phase diagrams, etc. were done by means of ThermoCalc software. The material database used was TCAL6 or TCAL7 along with MOBAL5 as mobility database. Each simulation mentions which ThermoCalc software version and database that have been used so that the results are clear to interpret. The software works with phase diagram calculations and mobility databases, which provide thermodynamic information such as Gibbs free energy, bulk diffusivity etc. Figure 21 illustrates the solidification simulations and precipitation simulations conducted for Al-Mn binary alloy system. Figure 21 a)-b) show the predicted Al-Mn binary phase diagram shows $Al_{12}Mn$ as the stable precipitate in the 500-800 K range and during solidification simulation, it is formed as stable precipitate at these temperatures. Upon isothermal simulation, as shown in Figure 21 c)-d), Al_6Mn is quickly stabilised into $Al_{12}Mn$. Several authors have claimed that Mn concentration of the alloy result in change of precipitation kinetics of Al_6Mn, $Al_{12}Mn$ over time during direct ageing [78, 79]. Additionally, the site for precipitation (bulk or grain boundaries) could provide different results during precipitation simulations. These differences were a part of validation experiments conducted when samples were heat treated at different temperatures and times. For example: when the precipitates were simulated to grow at grain boundaries instead of bulk of the sample using ThermoCalc, their sizes were approximately three times bigger within the same time scale, which is suggestive of faster growth at grain boundaries and that somewhat in agreement with experimental results.

In the present research work, the approach has also been to use self-defined models or literature for calculations and depiction of expected results, rather than relying completely on ThermoCalc. For example: prediction of strengthening of the Al-alloys were done with mathematical equations from literature such as solid solution strengthening [39, 40], shear hardening [47] and Orowan looping [48].

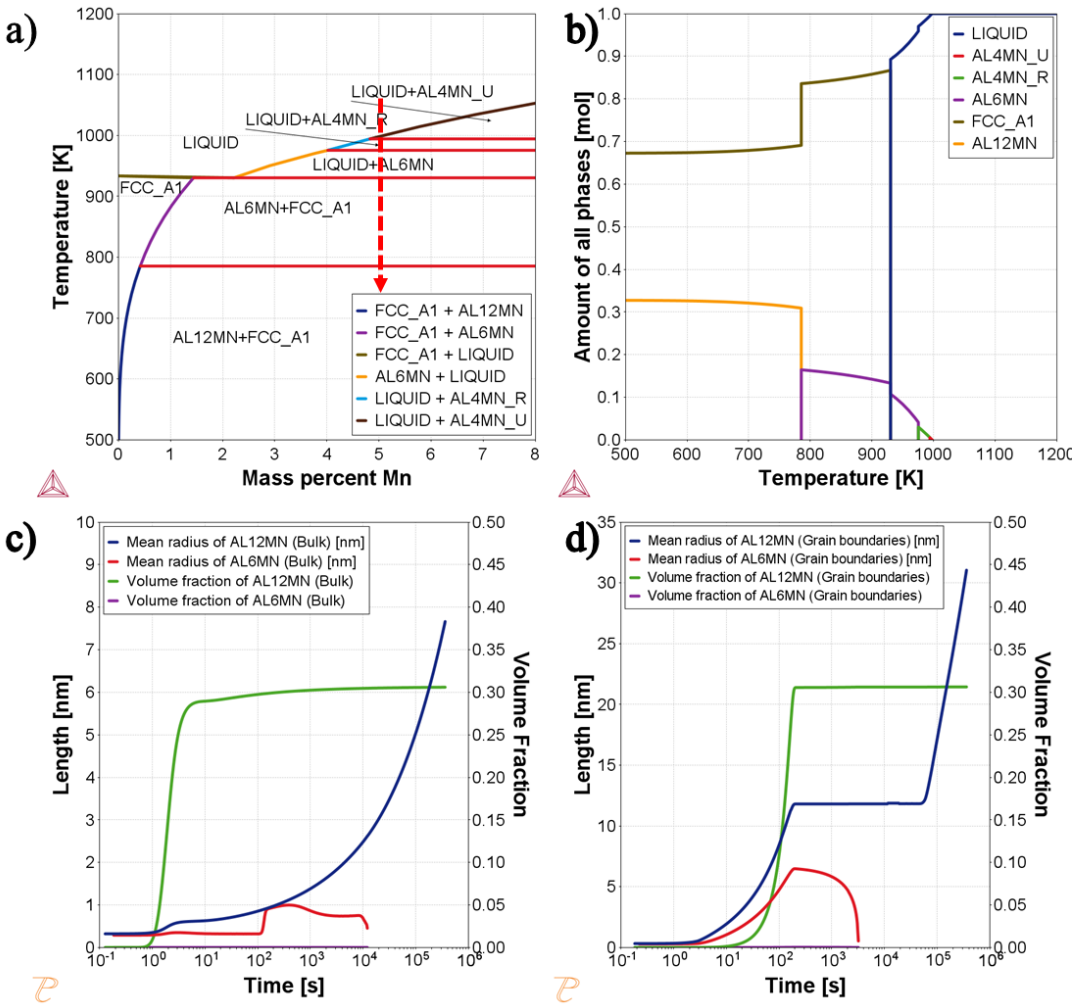

Figure 21 a) Al-Mn equilibrium phase diagram showing different phases formed b) Solidification simulation for Al-Mn binary alloy with 5wt% Mn, which follows the red dotted line in a). c),d) Isothermal precipitation reaction in Al-5 wt% Mn at 648 K when precipitates grow c) Bulk d) Grain boundaries. Notice how grain boundary precipitates grow about three times bigger in the same time. TCAL7 and MOBAL5 databases used on ThermoCalc 2021a to draw these curves.

3.4.2 Optical Microscopy

Light optical microscopy (OM) was applied using ZEISS Axioscope 7 instrument. The microscope is equipped with an automated stage, which makes it possible to create stitched version of images by selecting certain regions of interest. This was done with a 10X optical zoom for all the experiments where stitching was done, which provided a resolution of about 0.4 µm/pixel. This resolution was deemed good enough to detect pores with a size of about 1 µm. Pores smaller than this size were accepted as an error in density measurement. Smaller pores (<1 µm) were counted as fully-dense material.

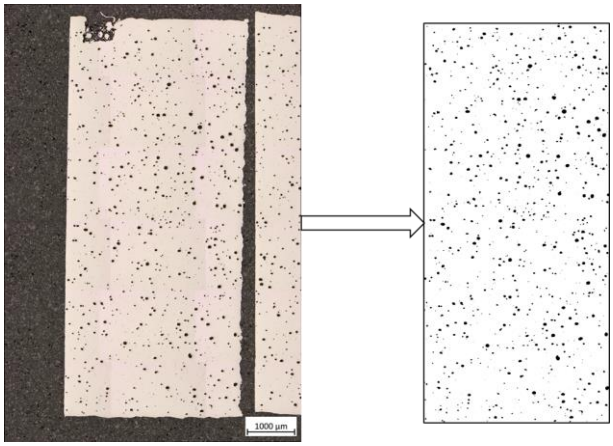

Figure 22 Left: light optical microscopy image of alloy C2 from one of the design of experiment along YZ cross section. The image was cropped, converted to 8-bit and thresholded (right) to analyse it using ImageJ software

As shown in Figure 22, the OM stitched images were processed using ImageJ version 1.52a. This software can help with taking large images to convert them into 8-bit data and later threshold the two extremes, being defects/porosities (black) and Al-matrix (white). Such image, after thresholding, was then subjected to analysing the area of black spots (pores) to calculate the relative density of the samples. This exercise was then repeated for all the samples across all three cutting planes and an average value was calculated for each sample. A usual stitched image from each sample did in this way represent a scanned area of 100-150 mm^2 which was deemed as a sufficient indicator of relative density.

3.4.3 Scanning Electron Microscopy

Scanning electron microscopy (SEM) was conducted as the basis for microstructural characterization. As shown in Figure 23 a), a typical SEM instrument produces an electron beam which is guided onto the sample using a separate lens system; the sample is mounted on a sample holder at a specific orientation depending on the analysis being conducted. The electron beam then interacts with the sample as shown in Figure 23 b), thus producing different types of electrons: Auger electrons (AE), secondary electrons (SE), back-scattered electrons (BSE) as well as characteristic X-rays. These reflected electrons are subsequently analyzed using detectors mounted on the machine, which provides information related to surface characteristics or chemical composition in the samples.

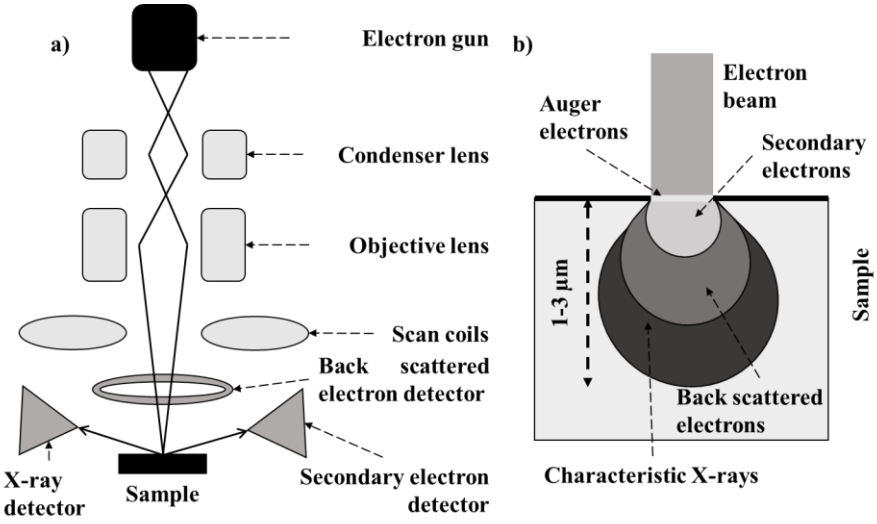

Figure 23 a) Schematic showing working principle of a typical scanning electron microscope setup b) Interaction volume created by electron beam into the sample with different type of electrons generated. Adapted from [80]

In this thesis study, a Leo Gemini Field Emission Gun 1550 SEM and Zeiss Gemini 450 SEM were used for imaging and chemical analysis. The microstructural analysis was conducted in combination with back scattered electron (BSE) detector to do the imaging and the X-ray energy dispersive spectroscopy (EDS) was employed for local chemical composition analysis. The Gemini 450 SEM is fitted with a Bruker Quantax FlatQuad EDS detector which could enable elemental mapping at low kV (<5 kV) by utilising L_α spectral lines along with K_α spectral lines. This was further enhanced by utilising AZtec software by Oxford Instruments, which could utilise feature analysis, by identifying precipitates as grey contrast in a certain image and develop a feature analysis map by collecting EDS point scans on detected features (in this case, the precipitates). This approach created a possibility to detect thousands of precipitates in a large area with resolutions up to ~0.1-0.15 µm along with chemical information, an example of what can be termed high throughput analysis. To limit map scanning to a maximum of 20 hours, it was decided to use 2 s as live exposure time (counts ~11000-12000) to detect EDS point scans. The SEM settings were selected as 4kV with 1 nA probe current; with this setup, the expected detectable spatial resolution was 0.12-0.13 µm. The imaging was done at 4096 resolution with minimum detection at 6 pixels, thus making a spatial resolution of 0.15 µm. However, EDS chemical analysis can still be considered semi-quantitative depending on various factors such as the thickness of interaction volume produced, orientation and cutting angle of the precipitate in the matrix, time of exposure of electrons etc., Figure 24 shows a SEM image before/ after feature analysis providing insight into how the software detects and later can classify different categories of precipitates based on morphology or chemistry.

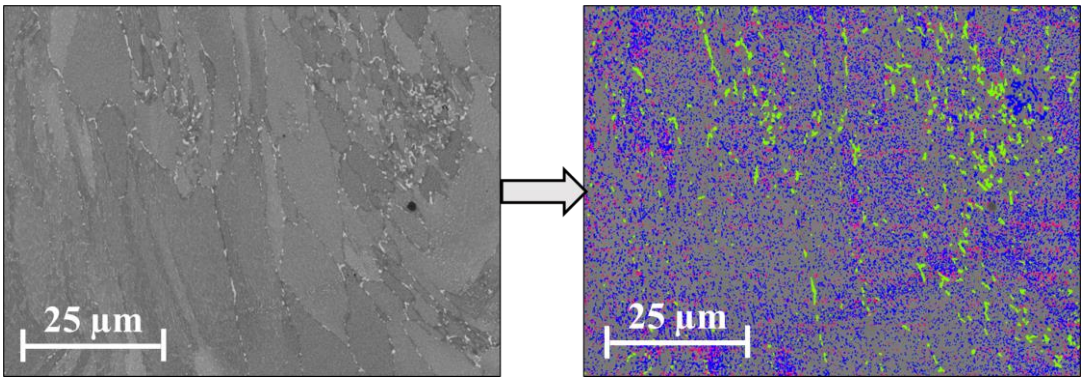

Figure 24 Feature analysis on Al-Mn-Cr-Zr alloy which is heat treated. It is shown that there is feature detection in image on the right with different colours representing different chemistry of Al-Mn precipitates detected from feature analysis. Pink: Matrix precipitates <5wt% Mn, Blue: $Al_{12}Mn$ precipitates 5wt%<Mn<20wt%, Green: Al_6Mn precipitates Mn>20wt%

3.4.4 X-ray Diffraction

X-Ray Diffraction (XRD) can be used as a tool for precipitation analysis and phase analysis. The XRD equipment generates X-rays beams which are directed on a crystalline sample. During this process, several nonparallel beams emerge from the sample. The angles at which beams emerge and their relative intensities provide information about lattice geometry, orientations, and arrangements of atoms in the crystal [81]. The identification of crystals is done using Bragg's law as shown in Equation 6.

$$n\lambda = 2d\sin\theta \tag{6}$$

The parameters in the equation above are as follows.

n	=	Diffraction order
λ	=	Wavelength of X-ray beam
d	=	Interplanar distance
θ	=	Diffraction angle

The diffraction planes that are observed can be compared to a database, such as the powder diffraction file (PDF) provided by International Centre for Diffraction Data (ICDD). For this thesis study, X-ray diffraction was employed at Höganäs AB to detect the phases formed in as printed and aged samples. Some kinetics studies were conducted to corroborate the diffusion out of solutes from the aluminium solid solution. The tests were conducted on samples finely ground till 2000 grit size on a Bragg-Brentano HD X-Ray machine equipped with a Cu source (Kα = 1.5406 Å) with 40 mA and 45 kV as the generator settings, scanned between 20°-100° 2Θ with a step size of 0.007° and scan step time as 68.59s. Some of the XRD patterns were analysed using DIFFRAC.SUITE EVA software by Bruker and the database used for pattern analysis was PDF-4+ 2020. The XRD plots were constructed using Origin 2020 software.

3.4.5 Chemical Analysis

Inductively Coupled Plasma Spectrometry (also called ICP-AES) was conducted on a SPECTRO ARCOS machine at Höganäs AB. It was done on all five alloys in as-atomised and as-printed condition. The purpose of this analysis was to detect chemical composition of all the alloys before and after printing, to identify exact chemical composition including impurities and also account for evaporation. The machine works by producing inductively coupled plasma that can excite atoms at wavelengths which can be used to detect elemental composition [82, 83].

3.5 Mechanical Testing

3.5.1 Hardness Testing

Hardness testing is conducted when an indenter, usually in the shape of pyramid or sphere and made from hard materials such as diamond makes an indentation on the sample surface at a defined load. This load is applied for a specified duration. After removing the load, the average diagonal length of the indentation along with the load applied provides an estimate of hardness of the sample. Vickers hardness (HV) tests were conducted on all the samples following the ASTM E384-17 standard [84]. As per the standard, Vickers Hardness can be calculated by following Equation 7.

$$\boldsymbol{HV = 1.8544.\frac{P_1}{d_1^2}} \tag{7}$$

The parameters in the equation above are as follows.

$\boldsymbol{HV}$	=	Vickers Hardness in HV
$\boldsymbol{P_1}$	=	Force, in kgf
$\boldsymbol{d_1}$	=	Mean diagonal length of the indentations, mm

Vickers hardness testing was conducted on all samples in a Durascan 70-G5 machine at 0.3 kg load and a hold time of 10 s. To comply with the ASTM standard, five times the indentation diagonal length was kept as minimum distance between two indentations and a total of 16 hardness indents (4 x 4 grid) each along XZ and XY plane were taken. These values were then presented as an average with one standard deviation as error bars.

3.5.2 Uniaxial Tensile Testing

Tensile testing was conducted on some of the samples at Höganäs AB. The testing was conducted following the ISO 6892-1:2019 standard [85] where cylindrical specimens were prepared with machined surfaces. The tests were conducted on a Zwick/ Roell 2100 machine with a 100 kN load cell. The extensometer used was with a 25 mm gauge length. The tests were conducted with crosshead speed control mode and speed was kept constant at 0.6 mm/min for the entire test.

Chapter 4 – Results and Discussion

This chapter presents a short summary of the results from the appended papers. Sections 4.1 and 4.2 discuss the basis of alloy design behind Al-Mn-Cr-Zr family of alloys and their printability. These two sections are described in detail in **paper I**. Section 4.3 discusses the effect of heat treatments on the microstructure of these Al-Mn-Cr-Zr alloys, particularly focusing on the precipitation kinetics of Al-Mn family of precipitates, which is discussed in **paper II**. Parts of section 4.1, 4.2 and section 4.4 discuss heat treatment and properties of Scalmalloy® , which constitute **paper III**.

4.1 Al-alloy Design Tailored for LB-PBF Process

As mentioned earlier in section 2.6.2, high supersaturation in the Al-matrix is possible via rapid solidification. Several authors [18, 17] have shown this concept to work with elements such as Sc and Zr with consistently good results and alloys are designed to achieve higher supersaturation of these elements. As per literature [39], it was found out that Mn, Cr and Fe are possible interesting elements that seem to have much higher solid solution hardening capabilities, as summarised in Figure 25. It was also shown during experiments done for hot sintering that up to 7.5 wt% Mn + Cr was soluble in powder condition with good properties in as-manufactured condition [74, 75]. Thus, based on literature and amount of supersaturations possible at LB-PBF cooling rates, alloying composition of 5.5 wt% Mn + Cr (total) were designed.

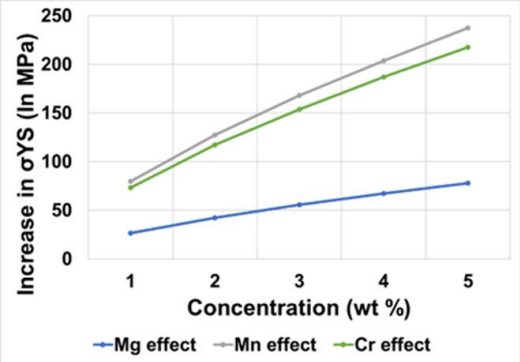

Figure 25 Solid solution strengthening effect from Mn, Cr as compared to Mg. It is seen that Mn, Cr have two-three times higher solid solution strengthening effect than Mg.

It was confirmed with XRD analysis, as summarised in **paper I** that the phases formed in as-atomised powder and as-printed material have a good dissolution of Mn, Cr and Zr, with minimum amount of secondary phase, confirmed as Al-Mn precipitates (<5 vol% as per phase intensity ratio). Additionally, the as-printed hardness values result of the alloys as shown in Table 7 showed significant increase in hardness as compared to pure-Al, thus proving the solid solution effect of Mn and Cr in the as-printed condition. The alloy design is kept flexible to add Mg later in order to create more grain refinement, as grain refinement effects in current state were moderate. Some authors have shown that the mechanism of having pre-cursor such as MgO can initiate formation of primary metastable Al_3Zr, which can cause grain refinement [18, 71].

Table 7 Vickers microhardness (HV0.3) for all four Al-Mn-Cr-Zr alloys in as-printed condition

Sample	Average value (HV)	Standard deviation (HV)
Alloy A	91.0	2.21
Alloy B	98.9	2.87
Alloy C1	103.4	3.21
Alloy C2	101.8	3.91

4.2 Printability Studies for Al-Mn-Cr-Zr Alloys and Al-Mg-Sc-Zr (Scalmalloy®)

Printability studies for Al-Mn-Cr-Zr family of alloys consisted of two parts. The first part concerned the theoretical printability of the Al-Mn-Cr-Zr alloys, which was calculated from Scheil solidification calculations done using ThermoCalc. As summarised in **Paper I** and shown in Figure 26, it was observed that the software predicted excellent printability due to a smaller solidification range along with a smaller slope $\left|\frac{dT}{d(f_s^{\frac{1}{2}})}\right|$ close to solidification, thus meaning that the segregations will not cause solidification cracking issues. It was later shown experimentally that the alloys had good printability with resistance to cracking, whereby no cracks were seen after printing several cubical samples. The second part addressed the details of experimental results conducted to achieve high density. This was done by varying laser speed and hatch distance while keeping laser power and layer thickness fixed. Surface plots were then derived after doing optical microscopy for polished samples along XY, XZ and YZ planes to measure relative density. Peak relative density of 99.4-99.6% was achieved for all four alloys demonstrating their good printability.

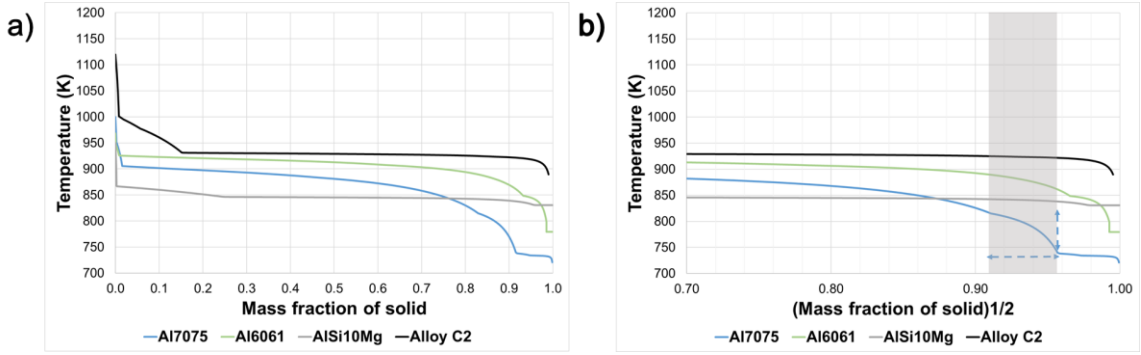

Figure 26 a) Scheil solidification curve for different Al-alloys across the whole solidification range. B) Scheil solidification curve when (mass fraction of solid)$^{1/2}$ is close to 1. The steepness of curve is illustrated for Al7075. Calculations done using ThermoCalc v2021a software using TCAL7 and MOBAL5 database.

Scalmalloy® was also tested using the same design of experiment approach and good results in terms of as-printed quality were also seen. A high-density processing parameter region (>99.5%) was identified and relative densities up to 99.8% were observed, as presented in **Paper III.** It was observed that no solidification cracks were present in the microstructure, although Mg is susceptible to segregation (shown in Figure 14). This is possible due to the grain refinement occurring in the Scalmalloy® material, leading to more favourable local solidification conditions to avoid solidification cracking issue altogether.

4.3 Al-Mn-Cr-Zr Alloys: Microstructure and Precipitation Kinetics

As summarised in **Paper I** and further developed in **Paper II**, the Al-Mn-Cr-Zr alloys are shown to have a typical columnar grain structure, which is found for several LB-PBF alloys [4, 7], see Figure 27. After direct ageing of the alloys between 573-678 K, it was seen that the Al-Mn families of precipitates are formed, selectively growing at grain boundaries as shown in Figure 28. However, tweaking the heat treatments after a few experiments, to apply temperatures of 623-648 K showed a secondary hardening behaviour, as summarised in the hardness maps in Figure 29. The hardness characteristic of this alloy family in aged condition is assumed to come from Al-Mn precipitates (especially the semi-coherent $Al_{12}Mn$ precipitates) via the Orowan looping mechanism and Al-Zr precipitates (nanometric coherent Al_3Zr precipitates) via the shearing mechanism. This hypothesis was the basis for doing further feature analysis, which is a special tool in the SEM using Aztec version 5.0 software. This tool depicted the precipitates via back scattered contrast in a large section area of the sample and did EDS point scans to

identify their composition within reasonable error (standard deviation ~2wt%). This method was thus used to explain the growth and chemistry of Al-Mn family of precipitates only. It was thus explained in **Paper II** that this alloy may have the possibility to control the precipitation and growth of Al-Mn precipitates, which are seen to shift from predominantly grain boundary precipitation to bulk precipitation between 14-24 hours at 648 K. It is hypothesised that this shift marks a particularly interesting condition in the heat treatment, as that also corresponds to the peak hardening capability of Al_3Zr precipitate. Owing to bulk growth of Al-Mn precipitates later during the heat treatment, it can be expected that the Al-Zr precipitate has a slow growth, thus providing a plateau of hardening response at such times. This effect can be leveraged for a good strength, indicated by the attained hardness value of 143-144 HV, see in Figure 29. It is expected that the hardness response on ageing this can be optimised further.

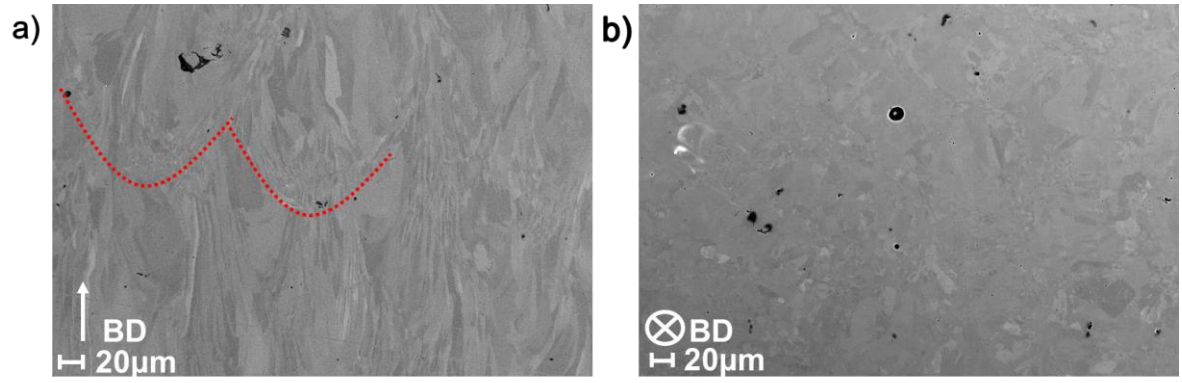

Figure 27 As printed microstructure of alloy C2 a) XZ section image showing bands of columnar grains and b) XY section image showing smaller grains.

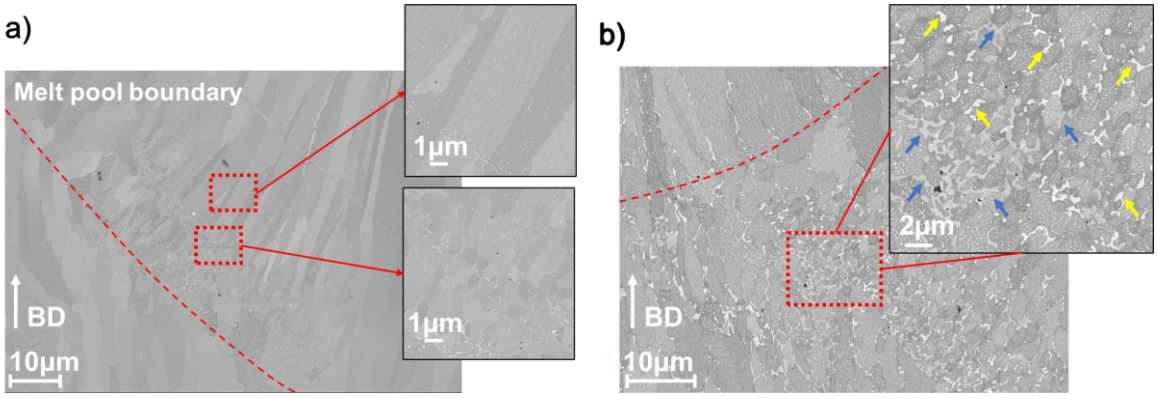

Figure 28 a) SEM image for as-printed sample of alloy C2 showing comparison difference in grain sizes for the regions where grain refinement occurs. Melt pool boundary is marked in red. b) SEM image for alloy C2 aged at 648 K 8 hours showing heavy precipitation at grain boundaries. The $Al_{12}Mn$ (darker contrast) precipitates are marked in blue whereas the Al_6Mn (brighter contrast) precipitates are marked in yellow.

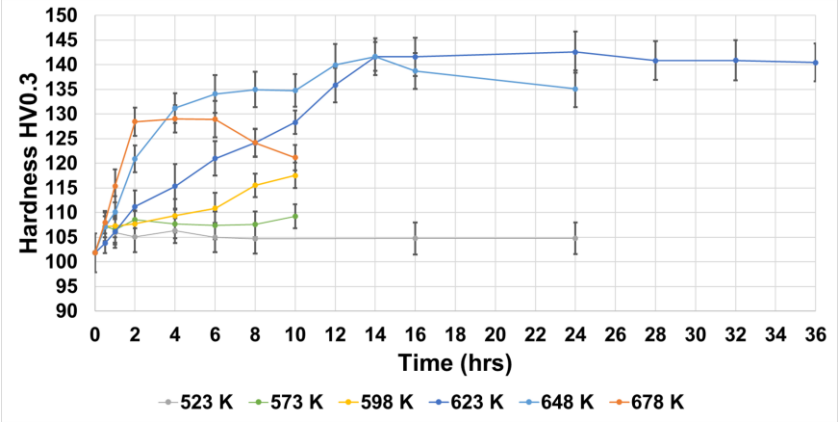

Figure 29 Vickers hardness (HV0.3) test for alloy C2 done at 523 K- 678 K at times varying between 0 and 36 hours for different temperatures. Hardness data is averaged for about 15 points each for XZ and XY directions and error bars represent one standard deviation.

4.4 Al-Mg-Sc-Zr (Scalmalloy®): Microstructure and High Temperature Properties

Paper III summarises the microstructure of as-printed Scalmalloy® seen to consist of equiaxed refined grain structure at melt pool boundaries, as shown in Figure 30. The grain sizes were seen to be less than 1 µm in these refined regions, which could be contributing to grain refinement strength in the as-printed and aged conditions. The heat treatment results summarised as hardness maps, along with tensile data for peak hardness (598 K for 4 hours), corresponded to results available in literature [17, 67]. This provides a good method for qualifying Al-alloys for new LB-PBF machines following a simple approach to achieve full density and high peak hardness property.

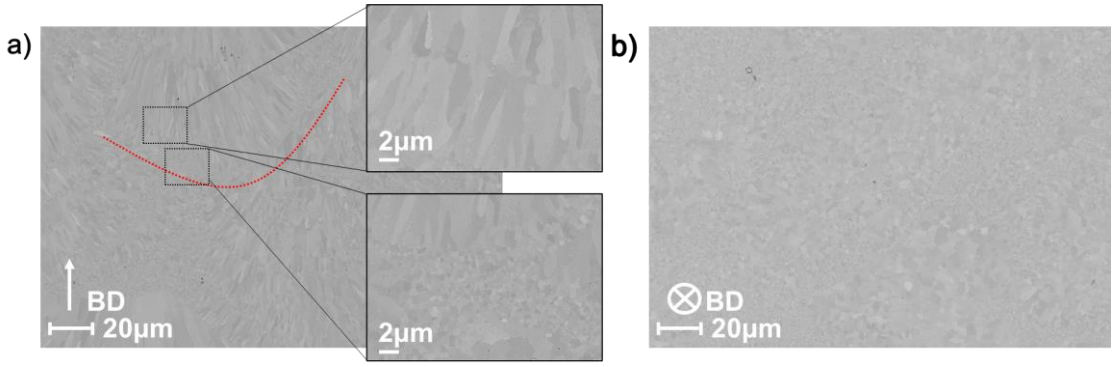

Figure 30 SEM images for Scalmalloy® showing as-printed microstructure a) XZ section showing refined grains at melt pool boundaries b) XY section showing small grains along transverse direction to build.

The second heat treatment was conducted after pre ageing the samples at 598 K for 4 hours and then post-processing ageing at three temperatures (423, 473, 523 K) between 0 and 120 hours and it was seen that little degradation in properties occurred, as opposed to what is mentioned by the results in [86]. Thus, it was concluded that longer times are needed to show actual degradation of high temperature properties (in order of thousands of hours).

Chapter 5 – Conclusions

Based on the results summarised in this thesis, some of the main conclusions are as follows:

Aluminium alloy design tailored for LB-PBF process is shown to be possible. Solidification cracking is normally expected to be a significant challenge during printing, but this can be avoided by screening the alloy compositions via simple Scheil solidification simulation or using other mechanisms, such as grain refiners. In this thesis, the former approach has been applied and this has also been combined within the scope of alloy design to take advantage of extended solid solubility using transition metal elements. Through the theoretical assessment of suitable alloys, it was depicted that some transition elements such as Mn, Cr and Zr are suitable candidates for alloying of aluminium to allow for LB-PBF processing. It was also depicted that high solid solubility far away from equilibrium solubility may be achieved via LB-PBF. In this thesis study, about 5.5 wt% Mn + Cr has shown to be printable with close to full solubility in as-printed condition. <5 vol% of primary precipitates were formed during printing, which is far from equilibrium (about 30 vol% $Al_{12}Mn$). The amount of Zr to be dissolvable is also around 0.6 wt%.

The precipitation kinetics for the new alloys developed relates to the two families of Al-Mn and Al-Zr compounds. The precipitates in Al-Mn family detected till now are of two types; $Al_{12}Mn$ precipitates (called G phase) which are hardening phases in the first stage and Al_6Mn precipitates observed over time, which are incoherent and possibly having limited hardening effect. The Al-Zr family forms Al_3Zr nanoprecipitates which is supposed to strengthen the matrix via shear hardening mechanism. It is shown in this thesis study that the Al-Mn family of precipitates appear to form and grow preferentially at grain boundaries, owing to supposedly faster transport of Mn along the grain boundaries. Over time, the experiments suggest that $Al_{12}Mn$ precipitates transform to Al_6Mn. However, this process is thought to change due to limited Mn availability and solubility limit of the matrix. When such a situation arises, the precipitation kinetics for the Al-Mn family shifts to the bulk diffusion control and $Al_{12}Mn$ precipitates can be said to grow slowly in the bulk of the sample. This means that now, higher strength may be achieved associated with secondary hardening. Furthermore, the Al-Zr precipitates are expected to grow via bulk diffusion and their growth kinetics can be fine-tuned to overlap with this shift of precipitation for the Al-Mn family. In this way, retention of its critical radius could be expected for longer time and thus preserved good strength.

The Scalmalloy® was shown to be printable in the same machine and approximate conditions as the newly developed Al-Mn-Cr-Zr alloy and shown to be heat treatable in good agreement with literature data. When high temperature performance for Scalmalloy® was explored by conducting secondary heat treatments, it was found out that such tests provided no evidence of the high temperature performance, unless the heat treatment times are increased by an order of magnitude. Furthermore, increasing the temperature to 473 K, the hardness values for Scalmalloy® appeared to deteriorate significantly, which could be a hinderance to high temperature applications.

To conclude, a new Al-Mn-Cr-Zr alloy family and an Al-Mg-Sc-Zr alloy tailored for LB-PBF process have been evaluated. With proper theoretical framework, the former alloy family has been developed and different variants of powder have been successfully printed without any solidification cracking. Moreover, the new alloy shows complex precipitation kinetics that have been started to be depicted in detail. The correlation and assessment of such kinetics as initiated in the present thesis study is supposed to contribute to an improved theoretical framework for development of new age-hardenable for LB-PBF. It is supposed that the precipitates formed could show low coarsening rates due to slow bulk diffusivities of the alloying elements, thus making the Al-Mn-Cr-Zr alloy variants a suitable candidate for high temperature applications. Owing to the possibility of tuneable properties that can be achieved via LB-PBF, such high-performance alloys could be a driver for adoption of AM as a technology for extended future applications.

Chapter 6 – Future Work

Future work is needed to develop the fundamentals behind the alloy development demonstrated. It was shown that the Al-Mn-Cr-Zr alloys are printable with negligible precipitations. However, the nanometric precipitates or possible chemical segregations at grain boundaries need to be explored. This may provide further insight into why Al-Mn precipitates grow preferentially at grain boundaries during ageing. Such information would also be important to shed further lights on the optimisation of the precipitate growth for best hardening effects. The Al-Zr precipitates need also to be characterized. There is good evidence in literature for formation of these precipitates, but the proposed microstructural development needs to be verified by high resolution electron microscopy conducted after different ageing times, whereby their tentative contribution towards alloy strength can be properly assessed.

The high temperature strength testing conducted for Scalmalloy® (Al-Mg-Sc-Zr alloy) were not representative of in-service conditions. The heat treatment studies performed showed that thousands of hours of ageing may be needed to develop high temperature property corelation. Hence, longer ageing studies for 2000-2500 hours are recommended for Scalmalloy® alloys as well as the newly developed Al-Mn-Cr-Zr alloys. Additionally, high temperature tensile tests would be of value, as long ageing times needs such tests to depict in-service condition.

Finally, the processing parameters have been tested on a smaller EOS M100 machine for cube specimens as well as some horizontal tensile test specimens. A more thorough investigation on a larger AM machine, such as the EOS M290 is recommended, along with printing of actual demonstrators to verify potential performance in applications. The assessment of relative density of the alloy along with studies on improving productivity, could be good way forward also to provide an idea about the alloy's flexibility to push build rates.

Acknowledgements

I would like to begin by acknowledging all three of my supervisors namely Prof. Lars Nyborg, Adj. Prof. Karin Frisk and Prof. Eduard Hryha for providing me with this exciting opportunity and introducing me to the world of research. I would acknowledge the funding from VINNOVA both through Centre for Additive Manufacturing- Metal (CAM^2) and ALL-Light (LIGHter network project) and support from Chalmers Production Area of Advance. The help from Adj. Prof. Sven Bengtsson and Sigurd Berg (from Höganäs AB) is highly appreciated as they helped with the alloy design discussions, patent process and providing atomized powder.

I would like to thank all the people who helped me with testing and analysis during the course of my licentiate; Arvid Svanberg for your great MSc thesis work; Ola Lyckfeldt, Anton-Dahl Jendelin, Sebastian Proper and Sepehr Hatami at RISE, Mölndal for help with experiments, collaborations and fruitful discussions; Björn Skårman, Dmitri Riabov at Höganäs AB for conducting XRD/ICP-AES experiments for me and help with interpreting them; Roger Sagdahl, Dr. Yiming Yao and Håkan Millqvist for helping with practical work at Chalmers, which I could not have figured out myself. My old office mate Elanghovan Natesan for guidance about how to navigate PhD life.

The acknowledgement extends to all the colleagues at IMS department, especially at AMPM group for all the great discussions and good times together. It is a fun place to work and the amount of diversity within research makes everything spicier (pun intended!) and I will cherish that going forward. Of course, thanks go to my friends in Sweden and India for making this experience over the last four years in a far-away land feel more like a second home. So, thanks to Fredrik, Erika, Richard, and Ismail for your support.

Finally, thanks to Jyo and my family for all your love in this long journey. We have come a long way, and I am grateful to have shared it with all of you.

References

[1] ISO International, "ASTM 52900: 2015 Additive Manufacturing," ISO International, 2015.

[2] C. Emmelmann, P.Sander, J.Kranz and E.Wycisk, "Laser Additive Manufacturing and Bionics: Redefining Lightweight Design," *Physics Procedia,* vol. 12, pp. 364-368, 2011.

[3] Y. Wang, L. Zhang, S. Daynes, H. Zhang, S. Feih and M. Y. Wang, "Design of graded lattice structure with optimized mesostructures for additive manufacturing," *Materials & Design,* vol. 142, pp. 114-123, 2018.

[4] T.DebRoy, H.L.Wei, J.S.Zuback, T.Mukherjee, J.W.Elmer, J.O.Milewski, A.M.Beese, A.Wilson-Heid, A.De and W.Zhang, "Additive manufacturing of metallic components – Process, structure and properties," *Progress in Materials Science,* vol. 92, pp. 112-224, 2018.

[5] M. Wang, T. Voisin, J. T. McKeown, J. Ye and N. Calta, "Additively Manufactured hierarchial stainless steels with high strngth and ductility," *Nature Materials,* vol. 17, pp. 63-70, 2018.

[6] A. S. Shaikh, F. Schulz, K. Minet-Lallemand and E. Hryha, "Microstructure and mechanical properties of Haynes 282 superalloy produced by laser powder bed fusion," *Materials Today Communications,* vol. 26, pp. 1-12, 2021.

[7] A. Leicht, C. Pauzon, M. Rashidi, U. Klement, L. Nyborg and E. Hryha, "Effect of part thickness on the microstructure and tensile properties of 316L parts produced by laser powder bed fusion," *Advances in Industrial and Manufacturing Engineering,* vol. 2, 2021.

[8] ASM International Handbook Committee, Aluminum and Aluminum Alloys, Materials Park, Ohio, US: ASM International, 1993.

[9] V.I.Elagin, "Ways of developing high-strength and high-temperature structural aluminum alloys in the 21st century," *Aluminum Alloys,* vol. 49, pp. 427-434, 2007.

[10] M. Tisza and Z. Lukacs, "High strength aluminum alloys in car manufacturing," in *IOP Conference Series: Materials Science and Engineering*, Ontario, 2018.

[11] S. Kou, "A criterion for cracking during solidification," *Acta Materialia,* vol. 88, pp. 366-374, 2015.

[12] J. Martin and B, "3D printing of high-strength aluminium alloys," *Nature,* vol. 549, pp. 365-369, 2017.

[13] T. Böllinghaus, H. Herold, C. E. Cross and J. C. Lippold, Hot cracking phenomena in welds II, Heidelberg: Springer, 2008.

[14] L. Thijs, K. Kempen, J.-P. Kruth and J. V. Humbeeck, "Fine-structure aluminium products with controllable texture by selective laser melting of pre-alloyed AlSi10Mg powder," *Acta Materialia,* vol. 61, pp. 1809-1819, 2013.

[15] I. Rosenthal, A. Stern and N. Frage, "Microstructure and Mechanical Properties of AlSi10Mg Parts Produced by the Laser Beam Additive Manufacturing (AM) Technology," *Metallography, Microstructure and Analysis,* vol. 3, pp. 448-453, 2014.

[16] EOS, "EOS Aluminium AlSi10Mg Material Data Sheet," 05 2021. [Online]. Available: https://www.eos.info/03_system-related-assets/material-related-contents/metal-materials-and-examples/metal-material-datasheet/aluminium/material_datasheet_eos_aluminium-alsi10mg_en_web.pdf. [Accessed 22 09 2021].

[17] K. Schmidtke, F. Palm, A. Hawkins and C. Emmelmann, "Process and Mechanical Properties: Applicability of a Scandium modified Al-alloy for Laser Additive Manufacturing," *Physics Procedia,* vol. 12, pp. 369-374, 2011.

[18] J. Croteau, S. Griffiths, M. Rossell, C. Leinenbach, C. Kenel, V. Jansen, D. Seidman, D. Dunand and N. Vo, "Microstructure and mechanical properties of Al-Mg-Zr alloys processed by selective laser melting," *Acta Materialia,* vol. 153, pp. 35-44, 2018.

[19] Q. Jia, P. Rometsch, P. Kurnsteiner, Q. Chao, A. Huang, M. Weyland, L. Bourgeois and X. Wu, "Selective laser melting of a high strength AleMneSc alloy: Alloy design and strengthening mechanisms," *Acta Materialia,* vol. 171, pp. 108-118, 2019.

[20] Q. Jia, F. Zhang, P. Rometsch, J. Li, J. Mata, M. Weyland, L. Bourgeois, M. Sui and X. Wu, "Precipitation kinetics, microstructure evolution and mechanical behavior of a developed Al–Mn–Sc alloy fabricated by selective laser melting," *Acta Materialia,* vol. 193, pp. 239-251, 2020.

[21] S. Thapliyal, M. Komarasamy, S. Shukla, L. Zhou, H. Hyer, S. Park, Y. Sohn and R. S. Mishra, "An integrated computational materials engineering-anchored closed-loop method for design of aluminum alloys for additive manufacturing," *Materialia,* vol. 9, 2020.

[22] H. Hyer, L. Zhou, A. Mehta, S. Park, T. Huynh, S. Song, Y. Bai, K. Cho, B. McWilliams and Y. Sohn, "Composition-dependent solidification cracking of aluminum-silicon alloys during laser powder bed fusion," *Acta Materialia,* vol. 208, 2021.

[23] D. L. Bourell, W. Frazier, H. Kuhn and M. Seifi, "Metal Additive Manufacturing Processes," in *ASM Handbook Volume 24- Additive Manufacturing Processes*, ASM International, 2020.

[24] EPMA, "Introduction to Additive Manufacturing," EPMA, 2019. [Online]. Available: https://www.epma.com/epma-free-publications/product/introduction-to-additive-manufacturing-brochure. [Accessed 23 09 2021].

[25] A. Ünal, "Effect of processing variables on particle size in gas atomization of rapidly solidified aluminium powders," *Materials Science and Technology (United Kingdom),* vol. 3, 1987.

[26] K. Riener, N. Albrecht, S. Ziegelmeier, R. Ramakrishnan, L. Haferkamp, A. B. Spierings and G. J. Leichtfried, "Influence of particle size distribution and morphology on the properties of the powder feedstock as well as of AlSi10Mg parts produced by laser powder bed fusion (LPBF)," *Additive Manufacturing,* vol. 34, 2020.

[27] A. Mussatto, R. Groarke, A. O'Neill, M. A. Obeidi, Y. Delaure and D. Brabazon, "Influences of powder morphology and spreading parameters on the powder bed topography uniformity in powder bed fusion metal additive manufacturing," *Additive Manufacturing,* vol. 38, 2021.

[28] A. Raza, T. Fiegl, I. Hanif, A. Markström, M. Franke, C. Körner and E. Hryha, "Degradation of AlSi10Mg powder during laser based powder bed fusion processing," *Materials & Design,* vol. 195, 2021.

[29] F. D. Re, V. Contaldi, A. Astarita, B. Palumbo, A. Squillace, P. Corrado and P. D. Petta, "Statistical approach for assessing the effect of powder reuse on the final quality of AlSi10Mg parts produced by laser powder bed fusion additive manufacturing," *The International Journal of Advanced Manufacturing Technology,* vol. 97, pp. 2231-2240, 2018.

[30] E. Hryha, R. Shvab, H. Gruber, A. Leicht and L. Nyborg, "Surface Oxide State on Metal Powder and its Changes during Additive Manufacturing: An Overview," in *Euro PM2017 Congress,* 2018.

[31] S. Kou, Welding Metallurgy, Second edition, Hoboken, New Jersey: John Wiley & Sons, Inc., 2003.

[32] J. Lippold, Welding Metallurgy and Weldability, Somerset: John Wiley & Sons Inc., 2014.

[33] M. Easton and D. StJohn, "Grain Refinement of Aluminum Alloys: Part I. The Nucleant and Solute Paradigms- A review of literature," *Metallurgical and Materials Transactions A,* vol. 30, pp. 1613-1623, 1998.

[34] A. M. Samuel and F. H. Samuel, "Effect of alloying elements and dendrite arm spacing on the microstructure and hardness of an Al-Si-Cu-Mg-Fe-Mn (380) aluminium die-casting alloy," *Journal of Materials Science,* vol. 30, pp. 1698-1708, 1995.

[35] M. A. M., F. L., R. F. Cochrane and N. J. Adkins, "Estimation of cooling rates during close-coupled gas atomization using secondary dendrite arm spacing measurement," *Metallurgical and materials Transactions B,* vol. 44, pp. 992-999, 2013.

[36] T. F. Bower, H. D. Brody and M. C. Flemings, "Measurements of solute redistribution in dendritic solidification," *Transaction of the Metallurgical Society of AIME,* vol. 236, pp. 624-633, 1966.

[37] D. G. Rogich and G. R. Matos, "The global flows of metals and minerals," 2008. [Online]. Available: http://pubs.usgs.gov/of/2008/1355/. [Accessed 04 12 2020].

[38] F. Ozturk, A. Sisman, S. Toros, S. Kilic and R. C. Picu, "Influence of aging treatment on mechanical properties of 6061 aluminum alloy," *Materials & Design,* vol. 31, no. 2, pp. 972-975, 2010.

[39] T. Uesugi and K. Higashi, "First-principles studies on lattice constants and local lattice distortions in solid solution aluminum alloys," *Computational Materials Science,* vol. 67, pp. 1-10, 2013.

[40] M. Walbruhl, D. Linder, J. Ågren and A. Borgenstam, "Modelling of solid solution strengthening in multicomponent alloys," *Materials Science and Engineering: A,* vol. 700, pp. 301-311, 2017.

[41] ASM, Heat Treating of Aluminium Alloys, ASM International, 1991.

[42] D. Dew-Hughes and W. D. Robertson, “The mechanism of hardening in aged aluminum-copper alloys,” *Acta Metallurgica,* vol. 8, no. 3, pp. 156-167, 1960.

[43] D.A.Porter and K.E.Easterling, Phase Transformations in Metals and Alloys, United Kingdom: Chapman & Hall, 1992.

[44] H. Sehitoglu, T. Foglesong and H. J. Maier, “Precipitate effects on the mechanical behavior of aluminum copper alloys: Part I. Experiments,” *Metallurgical and Materials Transactions A,* vol. 36, pp. 749-761, 2005.

[45] M. Albu, R. Krisper, J. Lammer, G. Kothleitner, J. Fiocchi and P. Bassani, “Microstructure evolution during in-situ heating of AlSi10Mg alloy powders and additive manufactured parts,” *Additive Manufacturing,* vol. 36, 2020.

[46] H. Qin, Q. Dong, V. Fallah and M. R. Daymond, “Rapid Solidification and Non-equilibrium Phase Constitution in Laser Powder Bed Fusion (LPBF) of AlSi10Mg Alloy: Analysis of Nano-precipitates, Eutectic Phases, and Hardness Evolution,” *Metallurgical and Materials Transactions A,* vol. 51, pp. 448-466, 2020.

[47] E. Nembach, “Precipitation hardening caused by a difference in shear modulus between particle and matrix,” *Physica Status Solidi (a),* vol. 78, no. 2, pp. 571-581, 1983.

[48] G.E.Dieter, Mechanical Metallurgy, New York: McGraw-Hill, 1986.

[49] A.J.Ardell, “Precipitation hardening,” *Metallurgical Transactions A,* vol. 16, pp. 2131-2165, 1985.

[50] M.A.Meyeres and K.K.Chawla, Mechanical metallurgy: principles and applications, Engelwood Cliffs: Prentice-Hall Inc., 1984.

[51] H.J.Frost and M.F.Ashby, Deformation-mechanism maps: the plasticity and creep of metals and ceramics, New York: Pergamon Press, 1982.

[52] Z. C. Cordero, B. E. Knight and C. A. Schuh, “Six decades of the Hall–Petch effect – a survey of grain-size strengthening studies on pure metals,” *International Materials Reviews,* vol. 61, no. 8, pp. 495-512, 2016.

[53] E.O.Hall, “The deformation and ageing of mild steel: III discussion of results,” *Proc. Phys. Soc.*, pp. 747-755, 1951.

[54] N. J. Petch, “The cleavage strength of polycrystals,” *Jorunal of Iron Steel Inst.*, vol. 174, pp. 25-28, 1953.

[55] R.K.Gupta, C. Mathew and P.Ramkumar, “Strain Hardening in Aerospace Alloys,” *Frontiers in Aerospace Engineering,* vol. 4, 2015.

[56] M. Pourbaix, Atlas of electrochemical equilibria in aqueous solutions, Houston: NACE Cobelcor, 1974.

[57] ThermoCalc, “CALPHAD Methodology,” ThermoCalc AB, [Online]. Available: https://thermocalc.com/about-us/methodology/the-calphad-methodology/. [Accessed 24 09 2021].

[58] T. E. Quested, A. T. Dinsdale and A. L. Greer, “Thermodynamic modelling of growth-restriction effects in aluminium alloys,” *Acta Materialia,* vol. 53, no. 5, pp. 1323-1334, 2005.

[59] N. Moleans, A. Miroux, E. Anselmino, S. v. d. Zwaag, B. Blanpain and P. Wollants, “Phase-field simulations of coarsening of Al6Mn precipitates located on grain boundaries in Al alloys,” in *TMS Annual Meeting and Exhibition*, 2009.

[60] H.-L. Chen, Q. Chen and P. Mason, “Assessments of Sc-Containing Ternary Systems Al–Sc–Ti and Al–Sc–Zr Within the Thermodynamic Database for Aluminium Alloys, TCAL5,” in *TMS Annual Meeting & Exhibition*, 2018.

[61] J. Allison, D. Backman and L. Christodoulou, “Intergrated computational materials engineering: A new paradigm for the global materials profession,” *Journal of The Minerals, Metals & Materials Society (TMS),* vol. 58, pp. 25-27, 2006.

[62] W. Y. Wang, J. Li, W. Liu and Z.-K. Liu, “Integrated computational materials engineering for advanced materials: A bried review,” *Computational Materials Science,* vol. 158, pp. 42-48, 2019.

[63] D. Wang, R. Shi, Y. Zheng, R. Banerjee, H. L. Fraser and Y. Wang, “Integrated Computational Materials Engineering (ICME) Approach to Design of Novel Microstructures for Ti-Alloys,” *Journal of Materials,* vol. 66, pp. 1287-1298, 2014.

[64] R. A. Michi, A. Plotkowski, A. Shyam, R. R. Dehoff and S. S. Babu, “Towards high-temperature applications of aluminium alloys enabled by additive manufacturing,” *International Materials Reviews,* 2021.

[65] Tesla Inc., “Aluminum alloys for die casting,” 06 02 2020. [Online]. Available: https://patentimages.storage.googleapis.com/6e/30/01/f25b5c31ffaed6/WO2020028730A1.pdf. [Accessed 28 09 2021].

[66] F. Yan, W. Xiong and E. J. Faierson, “Grain structure control of additively manufactured metallic materials,” *Materials,* vol. 10, no. 11, 2017.

[67] A. B. Spierings, K. Dawson, M. Voegtlin, F. Palm and P. J. Uggowitzer, “Microstructure and mechanical properties of as-processed scandium- modified aluminium using selective laser melting,” *CIRP Annals-Manufacturing Technology,* vol. 65, pp. 213-216, 2016.

[68] A. D. Pelton, G. Eriksson and C. W. Bale, “Scheil–Gulliver Constituent Diagrams,” *Metallurgical and Materials Transactions A,* vol. 48, pp. 3113-3129, 2017.

[69] P.Furrer and H.Warlimont, “Microstructure and properties of aluminum alloys after rapid solidification. Li. Extension of solid solubility, influence of thermal treatments, mechanical properties,” *Z. Fur. Met.,* pp. 100-112, 1971.

[70] Y. Du, Y.A.Chang, B. Huang, W. Gong, Z. Jin, H. Xu, Z. Yuan, Y. Liu, Y. He and F. Y. Xie, “Diffusion coefficients of some solutes in fcc and liquid Al: Critical evaluation and correlation,” *Materials Science and Engineering A,* vol. 363, pp. 140-151, 2003.

[71] S. Griffiths, M. D. Rossell, J. Croteau, N. Q. Vo, D. C. Dunand and C. Leinenbach, “Effect of laser rescanning on the grain microstructure of a selective laser melted Al-Mg-Zr alloy,” *Materials Characterization,* vol. 143, pp. 34-42, 2018.

[72] EU Commission, “Internal market, industry, entrepreneurship and SMEs,” 2020. [Online]. Available: https://ec.europa.eu/growth/sectors/raw-materials/specific-interest/critical_en. [Accessed 07 10 2021].

[73] Beamler Additive Manufacturing, “Scalmalloy: high performance aluminum for 3D printing,” Beamler Additive Manufacturing, 20 08 2020. [Online]. Available: https://www.beamler.com/scalmalloy-high-performance-aluminum-for-3d-printing/. [Accessed 07 10 2021].

[74] P. Liu, G. Dunlop and L.Arnberg, “Microstructural development in a rapidly solidified Al5Mn2.5Cr alloy,” *Materials Science and Engineering,* vol. 98, pp. 437-441, 1988.

[75] L. Arnberg, J. Lange and N. Bäckström, “Rapidly Solidified Ternary Al-Mn-Cr Alloys,” *Rapidly Quenched Metals,* pp. 919-922, 1985.

[76] Y. Y. Fan and M. M. Makhlouf, “Castable aluminium alloys for high temperature applications,” *Materials Science Forum,* pp. 8-12, 2013.

[77] Streurs, “Metallographic preparation of aluminum and aluminum alloys,” Streurs, [Online]. Available: https://www.struers.com/en/Knowledge/Materials/Aluminum#preparationmethod. [Accessed 29 09 2021].

[78] Y. Fan, K. Huang and M. M. Makhlouf, “Precipitation Strengthening in Al-Ni-Mn alloys,” *Metallurgical and Materials Transactions A,* vol. 46A, pp. 5830-5841, 2015.

[79] D. Shechtman, R. J. Schaefer and F. S. Biacaniello, “Precipitation in rapidly solidified Al-Mn alloys,” *Metallurgical Transactions A,* vol. 15, pp. 1987-1997, 1984.

[80] K. D. Vernon-Parry, “Scanning Electron Microscopy: An introduction,” *III-Vs review,* vol. 13, no. 4, 2000.

[81] K. H. Eckelmeyer, “X Ray Diffraction for Bulk Structural Analysis,” in *Metals Handbook,* ASM International, 1998.

[82] Spectro, “Spectro Arcos,” AMETEK, [Online]. Available: https://www.spectro.com/products/icp-oes-aes-spectrometers/arcos-inductively-coupled-plasma. [Accessed 28 09 2021].

[83] H. E. Taylor, Inductively Coupled Plasma-Mass Spectrometry, Boulder: Elsevier Inc., 2001.

[84] A. E384-17, Standard Test Method for Microindentation Hardness of Materials, West Conshohocken: ASTM International, 2017.

[85] A. E8/E8M, Standard Test Methods for Tension Testing of Metallic Materials, West Conshohocken: ASTM International, 2021.

[86] A. Plotkowski, K. Sisco, S. Bahl, A. Shyam, Y. Yang, L. Allard, P. Nandwana, A. M. Rossy and R. R. Dehoff, “Microstructure and properties of a high temperature Al–Ce–Mn alloy produced by additive manufacturing,” *Acta Materialia*, vol. 196, pp. 595-608, 2020.